JGR Solid Earth

RESEARCH ARTICLE
10.1029/2019JB019062

Quantifying the Relationship Between Short-Wavelength Dynamic Topography and Thermomechanical Structure of the Upper Mantle Using Calibrated Parameterization of Anelasticity

Fred D. Richards[1,2], Mark J. Hoggard[2,3], Nicky White[4], and Siavash Ghelichkhan[5]

[1]Department of Earth Science and Engineering, Imperial College London, London, UK, [2]Department of Earth and Planetary Sciences, Harvard University, Cambridge, MA, USA, [3]Lamont-Doherty Earth Observatory, Columbia University, Palisades, NY, USA, [4]Bullard Laboratories, Department of Earth Sciences, University of Cambridge, Cambridge, UK, [5]Research School of Earth Sciences, Australian National University, Acton, ACT, Australia

Key Points:
- Calibrated parameterization for anelasticity is used to convert upper mantle shear wave velocities into temperature, density, and viscosity
- Oceanic residual topography is dominated by ~100°C asthenospheric temperature anomalies and ±30 km lithospheric thickness deviations
- Revised approach helps to resolve amplitude discrepancies between observed and predicted dynamic topography at wavelengths <5,000 km

Supporting Information:
- Supporting Information S1

Correspondence to:
F. D. Richards,
f.richards19@imperial.ac.uk

Citation:
Richards, F. D., Hoggard, M. J., White, N., & Ghelichkhan, S. (2020). Quantifying the relationship between short-wavelength dynamic topography and thermomechanical structure of the upper mantle using calibrated parameterization of anelasticity. *Journal of Geophysical Research: Solid Earth*, *125*, e2019JB019062. https://doi.org/10.1029/2019JB019062

Received 18 NOV 2019
Accepted 1 JUL 2020
Accepted article online 6 July 2020

©2020. The Authors.
This is an open access article under the terms of the Creative Commons Attribution-NonCommercial-NoDerivs License, which permits use and distribution in any medium, provided the original work is properly cited, the use is non-commercial and no modifications or adaptations are made.

Abstract Oceanic residual depth varies on ≤ 5,000 km wavelengths with amplitudes of ±1 km. A component of this short-wavelength signal is dynamic topography caused by convective flow in the upper ~300 km of the mantle. It exerts a significant influence on landscape evolution and sea level change, but its contribution is often excluded in geodynamic models of whole-mantle flow. Using seismic tomography to resolve buoyancy anomalies in the oceanic upper mantle is complicated by the dominant influence of lithospheric cooling on velocity structure. Here, we remove this cooling signal from global surface wave tomographic models, revealing a correlation between positive residual depth and slow residual velocity anomalies at depths <300 km. To investigate whether these anomalies are of sufficient amplitude to account for short-wavelength residual depth variations, we calibrate an experimentally derived parameterization of anelastic deformation at seismic frequencies to convert shear wave velocity into temperature, density, and diffusion creep viscosity. Asthenospheric temperature anomalies reach +150°C in the vicinity of major magmatic hot spots and correlate with geochemical and geophysical proxies for potential temperature along mid-ocean ridges. Locally, we find evidence for a ~150 km-thick, low-viscosity asthenospheric channel. Incorporating our revised density structure into models of whole-mantle flow yields reasonable agreement with residual depth observations and suggests that ±30 km deviations in local lithospheric thickness account for a quarter of total amplitudes. These predictions remain compatible with geoid constraints and substantially improve the fit between power spectra of observed and predicted dynamic topography. This improvement should enable more accurate reconstruction of the spatiotemporal evolution of Cenozoic dynamic topography.

1. Introduction

It is generally agreed that oceanic residual depth provides a useful constraint on the present-day pattern of mantle convection (Cazenave et al., 1989; Flament et al., 2013; Menard, 1973; Panasyuk & Hager, 2000). Over the last decade, there has been a significant increase in the coverage of accurate spot estimates that are based upon analysis of modern and vintage seismic reflection and wide-angle refraction surveys (Czarnota et al., 2013; Hoggard et al., 2017; Winterbourne et al., 2009, 2014). Although this approach is not new, the quality and abundance of these surveys mean that corrections for sedimentary loading, for crustal thickness variation, and for lithospheric plate cooling can be carried out with greater accuracy. The resultant database of measurements can be used to investigate the spectral properties of topography that is generated by mantle flow (Davies et al., 2019; Hoggard et al., 2016; Steinberger et al., 2017; Yang & Gurnis, 2016). The recovered power spectrum has two notable features (Figure 1). First, the power at wavelengths that are longer than 5,000 km is up to 1 order of magnitude smaller than expected. Second, there is a significant and resolvable contribution at wavelengths that are shorter than 5,000 km.

Many predictive models of whole-mantle flow that exploit a mantle buoyancy structure derived from either global seismic tomography models or slab subduction histories have minimal spectral power at shorter wavelengths (Figure 1c; Flament et al., 2013). Since short-wavelength surface deflections are generated by buoyancy within the uppermost mantle, the existence of this spectral discrepancy suggests that buoyancy

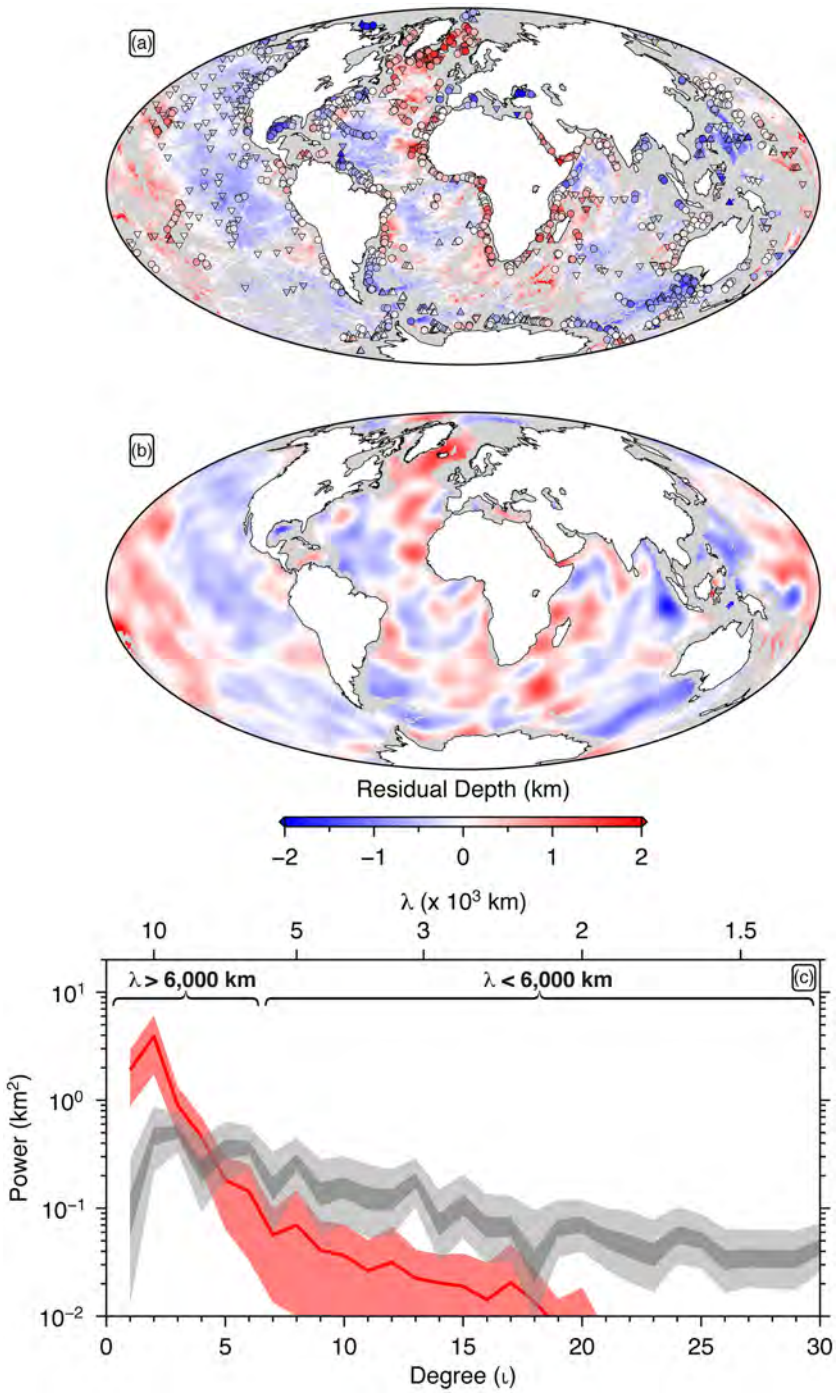

Figure 1. Global residual depth measurements. (a) Revised and augmented residual depth measurements (see also Hoggard et al., 2017). Circles = spot estimates corrected for both sedimentary and crustal thickness variations; up/down triangles = lower/upper bounds where crustal correction has not been applied; filigree pattern = estimates derived from shiptrack bathymetry and global sediment thickness grids alone (i.e., no crustal correction but major seamounts, fracture zones, and igneous provinces have been excised). All measurements are corrected for lithospheric cooling by assuming density structure of plate model at equivalent age (Richards et al., 2018). (b) Spherical harmonic representation of residual depth measurements for degrees $l = 1–30$ using method described by Hoggard et al. (2016). (c) Power spectra. Dark and light gray envelope = 99% and 50% confidence intervals about mean power spectrum of oceanic residual depth measurements constructed by Davies et al. (2019) using Automatic Relevance Determination algorithm; red line and envelope = mean power spectrum of surface deflections predicted by ensemble of five whole-mantle flow models and its $\pm 1\sigma$ standard deviation (Conrad & Husson, 2009; Flament et al., 2013; Ricard et al., 1993; Spasojevic & Gurnis, 2012; Steinberger, 2007).

contributions from $\leq$ 300 km depth are probably underestimated (Hoggard et al., 2016). Many, but not all, flow models ignore density anomalies that are shallower than this depth, partly because of the difficulty in reliably converting seismic velocity into density at these depths, which reflects uncertainties in the magnitude of anelastic effects (Flament et al., 2013).

Improvements in the quantity of seismograms, in inverse modeling techniques, and in computational power have led to a steady increase in the resolution of seismic tomographic models. Many of these models now show that there is a significant contribution from short-wavelength velocity anomalies within the uppermost mantle that generally dies out with depth. These developments suggest that the lithosphere and asthenosphere probably host significant lateral variations of temperature and composition at these shorter length scales (Becker, 2002). Indeed, recent predictive models of mantle flow that attempt to incorporate upper mantle structure yield a spectral power distribution that is more consistent with estimates from residual topography (Davies et al., 2019; Steinberger, 2016; Steinberger et al., 2017). However, these revised models consistently overpredict the amplitude of short-wavelength surface deflections by up to a factor of 2. Furthermore, it remains unclear whether this short-wavelength residual depth variation is primarily generated by buoyancy anomalies within the sub-plate mantle or by local deviations in lithospheric thickness that depart from the average cooling trend (Davies et al., 2019). These remaining issues emphasize the need to develop accurate conversions from seismic velocity into upper mantle density structure.

In this study, we address how this short-wavelength spectral discrepancy between residual depth estimates and predictions from mantle flow simulations might be resolved. First, the spatial correlation between upper mantle shear wave velocities and residual depth is analyzed. Second, a revised plate cooling model is combined with a range of constraints on mantle temperature, viscosity and attenuation in order to calibrate an experimentally derived anelastic parameterization for converting shear wave velocity into temperature and density. The resultant temperature estimates are tested against independent geophysical and geochemical observations. The calculated density variation is used to assess the extent to which residual depth measurements can be accounted for by asthenospheric temperature anomalies, by lithospheric thickness changes, and by large-scale mantle flow. Finally, we are conscious that there is an ongoing debate concerning the precise definition of dynamic topography (Braun, 2010; Forte et al., 2010; Gvirtzman et al., 2016; Hoggard et al., 2020a; Molnar et al., 2015). As in previous studies, we are interested in exploiting residual depth measurements from oceanic plates. These estimates include a correction for lithospheric isostasy that implicitly assumes that, for seafloor of a given age, a plate cooling model yields a good approximation of the subsurface mantle density structure. Thus, observed residual depth variations may be generated by a combination of sub-plate convection plus local departures from the average age-dependent thermal structure. This latter contribution is generally considered to be a form of isostasy and can originate either from deviations in lithospheric thickness or temperature anomalies that reside within the plate. To facilitate comparison between residual depth estimates and predictions obtained from our revised mantle density structure, here we have included all these potential sources of anomalous buoyancy in our definition of dynamic topography.

2. The Short-Wavelength Spectral Discrepancy

Richards and Hager (1984) showed that, if Earth's viscosity varies as a function of radius alone, a spectral approach can be used to predict deflections of the free surface, core-mantle boundary, and geoid that are generated by flow-driven density anomalies within the mantle. Using the propagator matrix technique, equations governing conservation of mass and momentum within a highly viscous spherical shell are solved alongside Poisson's equation to generate a suite of sensitivity kernels, which vary as a function of radius and spherical harmonic degree, l (Figure 2). Normalized surface topography kernels, $A^l(r)$, where r is radial distance, are used to compute the deflection of the Earth's surface, δa^{lm}, by solving

$$\delta a^{lm} = \frac{1}{\Delta\rho}\int_r^{R_\oplus} -A^l(r)\delta\rho^{lm}(r)dr \tag{1}$$

where m is spherical harmonic order, $\Delta\rho$ is the density difference between mantle and overlying fluid (i.e., air or water), $R_\oplus = 6{,}371$ km is the radius of the Earth, and $\delta\rho^{lm}(r)$ represents the driving mantle density anomalies. The relationship between l and wavelength, λ, is given by the Jeans relations where

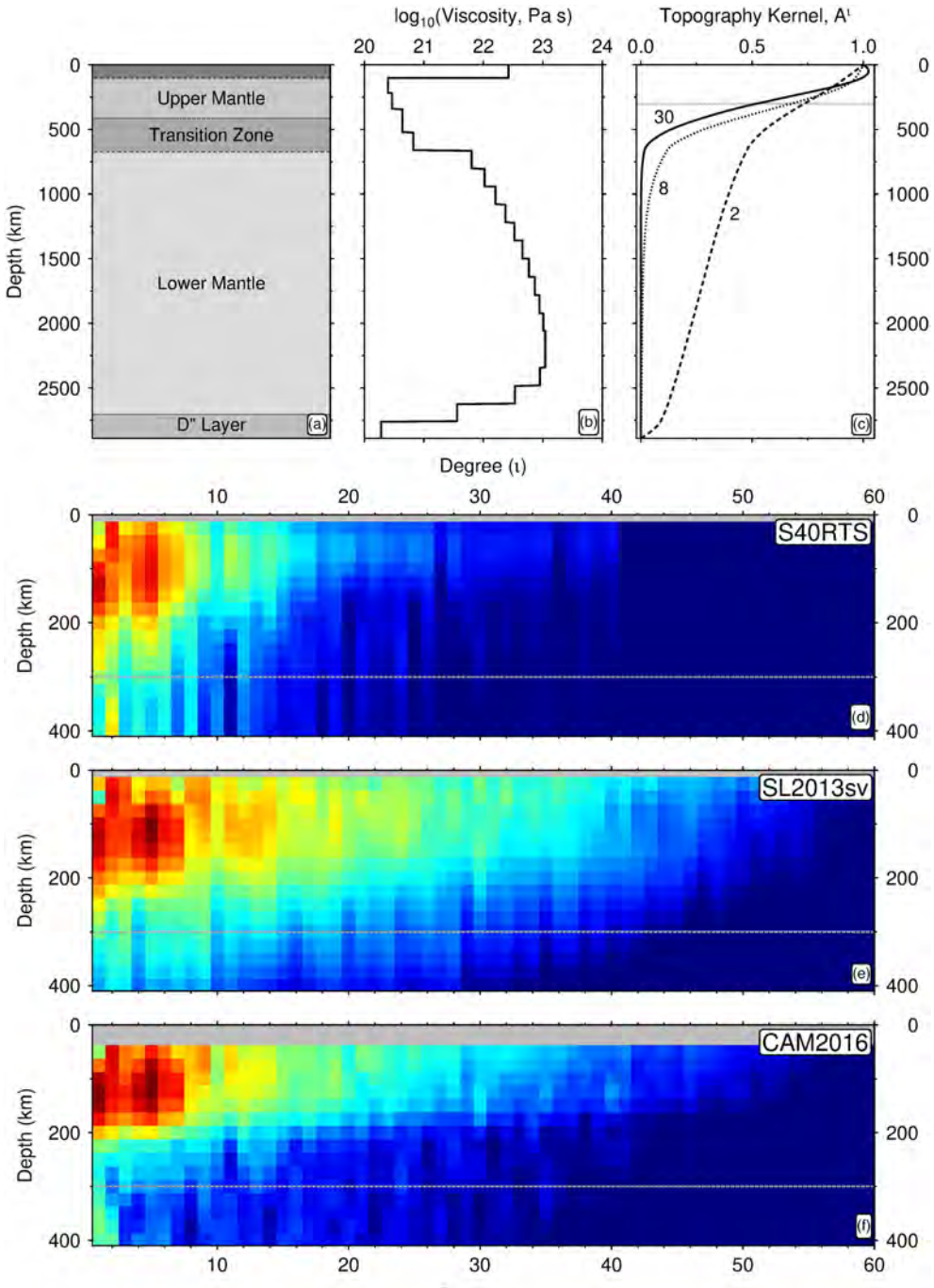

Figure 2. Instantaneous flow kernels and seismic tomographic spectra. (a) Generalized radial mantle structure. (b) Radial viscosity profile as a function of depth taken from Steinberger et al. (2010). (c) Normalized surface response kernels as a function of depth for viscosity profile shown in panel (a) and calculated using method described by Corrieu et al. (1995). Horizontal dashed line = ~300 km, the depth above which density anomalies are typically excluded in models of whole-mantle flow (Flament et al., 2013). Numbers = selected spherical harmonic degrees. (d) Power spectrum of isotropic shear wave velocity anomalies, V_S, as a function of depth and degree for S40RTS model (Ritsema et al., 2011). (e) Same for vertically polarized shear wave velocity anomalies, V_{SV}, from SL2013sv model (Schaeffer & Lebedev, 2013). (f) Same from CAM2016 model (Ho et al., 2016).

$$\lambda = \frac{2\pi R_{\oplus}}{\sqrt{l(l+1)}} \tag{2}$$

Spherical harmonic degrees $l = 2$, 8, and 30 correspond to wavelengths of approximately 15,000 km, 4,700 km, and 1,300 km, respectively. Normalized surface topography kernels for these three values of l,

assuming the radial viscosity model of Steinberger et al. (2010), are shown in Figure 2c. The exact shapes of these functions depend upon relative steps of viscosity but the greatest sensitivity to density for any value of l occurs at the surface. For larger values of l (i.e., shorter wavelengths), this sensitivity is increasingly concentrated within the shallow mantle.

Surface dynamic topography is usually calculated from an inferred density structure by iteratively updating the radial viscosity profile until the misfit between observed and calculated geoid height anomalies is minimized (Hager et al., 1985). Density structures are typically inferred by scaling the velocity anomalies of a given seismic tomographic model, although slab subduction histories obtained from plate reconstructions have also been exploited (Ricard et al., 1993; Spasojevic & Gurnis, 2012). Significantly, many predictive flow models exclude density anomalies within the top ~300 km of the mantle for three reasons. First, simple temperature-based velocity-to-density conversions in this depth range are complicated by significant anelastic effects and by compositional differences between thick cratonic roots and fertile oceanic upper mantle (Jordan, 1975; Karato, 1993; Yamauchi & Takei, 2016). Second, lithospheric thickness changes are associated with lateral viscosity gradients, which calls into question the validity of one-dimensional radial viscosity profiles and poses computational difficulties for three-dimensional numerical simulations (Osei Tutu et al., 2018; Zhong & Davies, 1999). Third, global whole-mantle tomographic models tend to have minimal short-wavelength structure within the uppermost mantle due to the low density of crossing ray paths (Bodin et al., 2015; Ritsema et al., 2011).

It is evident from the shape of the sensitivity kernels shown in Figure 2c that neglecting mantle density anomalies which are shallower than 300 km will tend to preferentially penalize short-wavelength (i.e., $l = 8$–30) contributions to dynamic topography. Moreover, most global seismic tomographic models have only modest spectral power for $l>8$ in this depth range (Figure 2d). In contrast, upper mantle tomographic models that are constructed primarily from surface wave data recover substantially more structure, with significant spectral power extending out to $l\sim50$ (i.e., wavelengths down to ~800 km; Figures 2e and 2f). Thus, omission of the shallow mantle and use of density structures derived from whole-mantle seismic tomography models will inevitably lead to mantle flow predictions that underestimate short-wavelength surface deflections. Correctly accounting for shallow mantle density anomalies is therefore essential for addressing the spectral discrepancy between oceanic residual depth and mantle flow predictions at wavelengths that are shorter than 5,000 km.

3. Correlating Residual Depth Anomalies and Seismic Tomography

In recent decades, a combination of theoretical advances, growing computational power, and improved data coverage have spurred the development of increasingly sophisticated, higher resolution seismic tomographic models. In particular, models have been developed that are primarily constructed from surface waves, including fundamental modes and overtones, which are particularly sensitive to upper mantle structure (Debayle et al., 2016; French et al., 2013; Priestley et al., 2012; Schaeffer & Lebedev, 2013). The upper mantle is sampled by a greater number of crossing ray paths, leading to typical vertical resolution of 25–50 km, and a horizontal resolution of 200–600 km. These inversions also tend to be less strongly regularized than whole-mantle equivalents and generally recover velocity anomalies with larger amplitudes. Hence, they have the potential to image buoyancy anomalies that are responsible for observed short-wavelength residual depth variations ($8 \leq l \leq 30$; $5,000\ \text{km} \leq \lambda \leq 1,000\ \text{km}$.

Analyzing continental residual topography is not straightforward since their protracted geologic histories and significant chemical heterogeneity have resulted in a complex buoyancy structure that is difficult to model and remove (Jordan, 1978). In contrast, the thermochemical structure of oceanic lithosphere appears to be significantly simpler and is well understood (Parsons & Sclater, 1977; Richards et al., 2018).

Within the upper mantle of the oceanic realm, seismic tomographic images are dominated by the platecooling signal, making it difficult to identify velocity anomalies associated with sub-plate buoyancy (Figures 3a and 4a). We therefore attempt to isolate these features by stripping out the seismic velocity structure associated with age-dependent thickening of oceanic lithosphere, thereby generating a model of "residual tomography" (Wen & Anderson, 1997). This process involves generating a global stack of oceanic seismic velocities as a function of depth and lithospheric age for each tomographic model. First, anomalous regions of oceanic lithosphere, which include major fracture zones, seamounts and large igneous provinces, are

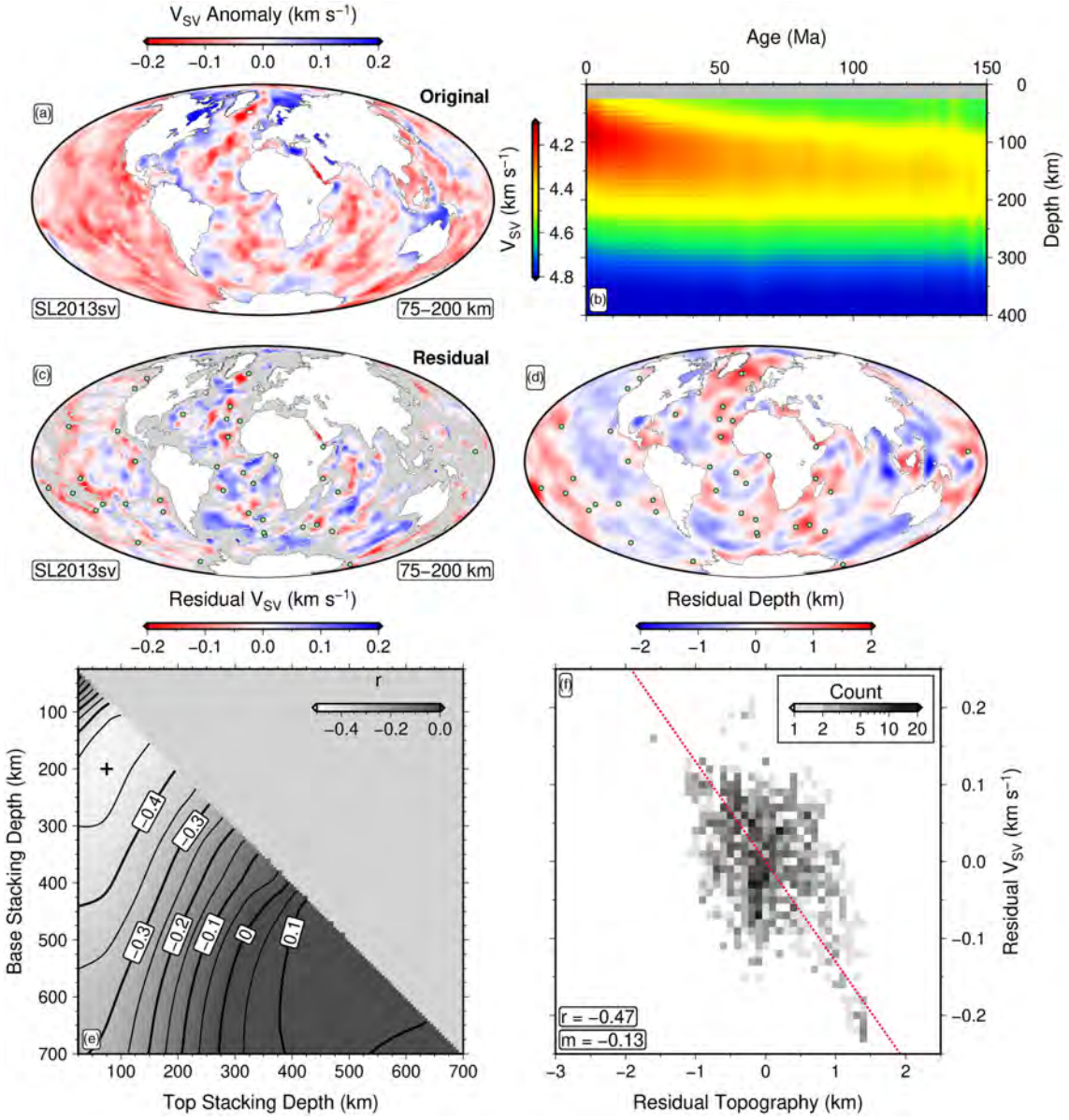

Figure 3. Comparison between residual depth measurements and residual tomography from SL2013sv model (Schaeffer & Lebedev, 2013). (a) Shear wave velocity anomalies vertically averaged between depths of 75 km and 200 km. (b) Global stack showing average variation of V_{SV} as a function of depth and plate age, excluding regions with anomalous oceanic crust (e.g., fracture zones, seamounts, and large igneous provinces; Hoggard et al., 2017). (c) Residual shear wave velocity anomalies vertically averaged between depths of 75 km and 200 km; green circles = magmatic hot spots; gray shading = regions with anomalous oceanic crust. (d) Spherical harmonic representation of oceanic residual depth measurements from Figure 1b. (e) Pearson's correlation coefficient, r, between residual depth measurements and residual velocities as a function of top and base stacking depths (i.e., depth range over which residual velocities have been vertically averaged); black cross = locus of optimal value. (f) Correlation between spot residual depth measurements and residual V_{SV} for optimal stacking depth range between 75 km and 200 km. $r = -0.47$; red line = best-fitting linear relationship with slope of $m = -0.13$.

excised using the exclusion polygons of Hoggard et al. (2017). Second, the revised oceanic crustal age grid of Richards et al. (2018) is used to subdivide the principal oceanic basins into 2 Myr bins. Third, a V_{SV} profile is extracted for each location within a given bin and stacked to yield the mean and standard deviation of V_{SV} as a function of age and depth (Figures 3b and 4b). Finally, the resulting average velocity structure at any given age is removed from each local velocity profile to generate maps of residual velocity. In this way, individual depth slices can be vertically averaged over many different combinations of top and basal depths to investigate the depth extent of residual velocity anomalies. This process identifies coherent signals that

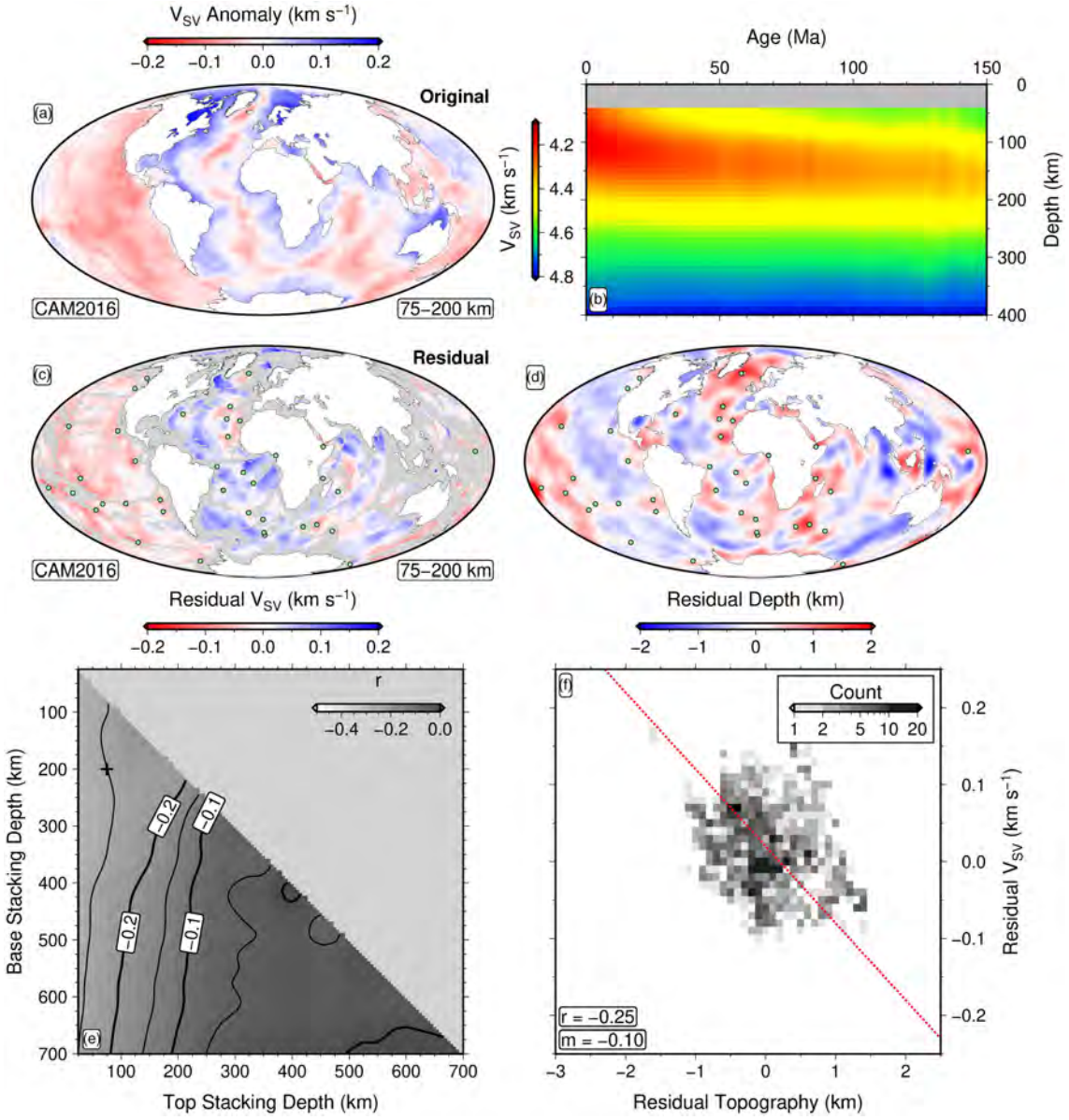

Figure 4. Comparison between residual topography and residual tomography based on CAM2016 model (Ho et al., 2016). Panels same as for Figure 3.

are consistently different to average plate cooling trends. We observe that slow and fast residual velocity anomalies consistently underlie positive and negative residual depth anomalies, respectively (Figures 3c and 4c). This visual relationship is compatible with the expectation that observed buoyancy anomalies are principally of thermal origin, given that seismic velocities are inversely dependent on temperature (Figures 3d and 4d; Hoggard et al., 2016).

To investigate the depth extent of mantle anomalies that control this relationship, we have expanded both residual velocity and residual depth anomalies up to $l = 30$. The resultant grids were then point-wise sampled at locations where spot estimates of residual depth anomalies occur. The optimal spatial correlation for the SL2013sv model of Schaeffer and Lebedev (2013) occurs when residual tomography is stacked over a depth range of 75–200 km ($r = -0.47$; Figures 3e and 3f). This depth range coincides with the approximate thickness of a low-viscosity asthenospheric channel that has been inferred from observations of glacial isostatic adjustment, from post-seismic rebound analysis, from studies of seismic anisotropy, and from plate motion force balance calculations (Hu et al., 2016; Iaffaldano & Lambeck, 2014; Lin et al., 2016; van der

Wal et al., 2015). We note that 95% of known magmatic hot spots occur within 200 km of slow residual shear wave velocity anomalies. Some of the scatter in the relationship between residual tomography and residual depth could reflect either compositional variations within the oceanic mantle or the contribution of deeper mantle flow to surface deflections (Colli et al., 2016; Dalton et al., 2014). Nevertheless, the overall correlation between upper mantle residual tomography, residual depth, and intraplate volcanism suggests that the SL2013sv model resolves asthenospheric temperature anomalies on wavelengths that are as short as ~1,000 km.

Similar results have been obtained for other tomographic models, although correlations between residual tomography and residual depth are generally poorer. For example, analysis of the CAM2016 model finds a weak correlation between 75 km and 200 km ($r = -0.25$; Figures 4e and 4f; Ho et al., 2016). The SEMUM2 model of French et al. (2013) yields $r = -0.39$, which is similar to that obtained for the SL2013sv model over the same depth range. The PM2012 and 3D2015_07Sv models yield r values of −0.28 and −0.20, respectively (Debayle et al., 2016; Priestley et al., 2012). These values are roughly equivalent to those obtained for the S362ANI model, which exploits a larger proportion of body waves ($r = -0.23$; Kustowski et al., 2008). In general, better correlations are obtained for tomographic models that are predominantly constructed from surface wave observations and exploit large quantities of higher mode information. We suggest that the success of the SL2013sv model can be attributed to two distinguishing features. First, their inverse procedure allows the initial crustal velocity model to be iteratively updated rather than it being kept fixed. Second, a significant quantity of higher mode information is incorporated while simultaneously including large numbers of quality-controlled seismograms. This visual comparison illustrates the existence of upper mantle anomalies with the correct spatial pattern. We next explore whether these features are sufficiently large to account for missing sources of buoyancy that could support short-wavelength variations in residual topography.

4. Relationships Between Shear Wave Velocity, Temperature, and Density

To assess the magnitude of upper mantle buoyancy anomalies, we require a method for converting shear wave velocities into temperature and density. Several recent geodynamic studies have used constant or depth-dependent linear scalings to carry out this conversion and typically overestimate the amplitude of short-wavelength residual depth by up to a factor of two (e.g., Davies et al., 2019; Steinberger, 2016, 2017). A component of this mismatch is likely to be related to the effect of anelasticity on shear wave velocity at seismic frequencies. At low temperatures, the propagation of seismic energy occurs primarily by elastic deformation of mantle minerals and this "anharmonic" velocity has an approximately linear dependence upon temperature and pressure (Kumazawa & Anderson, 1969). However, as temperature increases toward the solidus, anelastic deformation (i.e., fully recoverable but time-dependent strain) starts to occur, which leads to dissipation of seismic energy and an additional reduction in seismic velocity (Cammarano et al., 2003; Karato, 1993). As a result of these anelastic effects, the relationship between shear wave velocity, temperature, and density can be highly non-linear even at a fixed depth.

4.1. Parameterization of Anelasticity at Seismic Frequencies

Several models of anelasticity have been proposed for the upper mantle that are based upon the results of forced oscillation experiments carried out on either pure olivine or polycrystalline analogs (Faul & Jackson, 2005; Jackson et al., 2010; McCarthy & Takei, 2011; Yamauchi & Takei, 2016). Olivine-based experiments have the advantage of being compositionally similar to the upper mantle. Unfortunately, in order to achieve textural equilibrium on laboratory timescales, samples have very small grain sizes (i.e., <50 μm). Consequently, grain size relationships must be extrapolated over 3 orders of magnitude to approximate the expected grain size at upper mantle conditions (i.e., 5–10 mm; Jackson et al., 2014). Alternatively, experiments on compositionally dissimilar polycrystalline analogs can be carried out at more representative grain sizes (Holtzman, 2016). An organic compound called borneol is often used in studies of anelasticity since it forms a simple binary eutectic system with diphenylamine that exhibits similar equilibrium microstructures to the olivine-basalt system (McCarthy et al., 2011).

McCarthy et al. (2011) demonstrated that there is a broad similarity in the anelastic responses of borneol and olivine provided that measurements are scaled using the Maxwell frequency, $f_M = \frac{\mu_U}{\eta}$, of each material,

where μ_U is the unrelaxed shear modulus and η is the diffusion creep viscosity. Priestley and McKenzie (2013) exploited this scaling relationship to show that a representative range of independent shear wave velocity, attenuation and viscosity measurements could be adequately fitted using a single set of material properties that are broadly consistent with independent experimental values. At that time, the lack of laboratory experiments carried out at seismic frequencies meant that calibration of their anelastic model required extrapolation of the Maxwell frequency scaling relationship up to the seismically relevant normalized frequency band of $10^6 \leq \frac{f}{f_M} \leq 10^9$. However, the resultant parameterization predicted an insufficient decrease in shear wave velocity at near-solidus conditions to match observations from oceanic lithosphere. This shortcoming was remedied through the inclusion of an abrupt drop in viscosity by a factor of 100 at the solidus (Priestley & McKenzie, 2013). Subsequently, Takei et al. (2014) showed that, at these higher frequencies, the simple Maxwell frequency scaling relationship breaks down and an additional term must be added to this "high-temperature background" trend in order to adequately match the experimental observations. This term accounts for the rapid decrease in shear wave velocity observed close to the solidus. The predicted attenuation is also more consistent with independent oceanic observations over relevant temperature and depth ranges (Yamauchi & Takei, 2016). We therefore adopt the parameterization of Yamauchi and Takei (2016) in this study. The shear wave velocity, V_S, is given by

$$V_S = \frac{1}{\sqrt{\rho J_1}}\left[\frac{1+\sqrt{1+(J_2/J_1)^2}}{2}\right]^{-\frac{1}{2}} \simeq \frac{1}{\sqrt{\rho J_1}} \tag{3}$$

where ρ is density. J_1 and J_2 represent real and imaginary components of the complex compliance, J^*, which is a quantity describing the sinusoidal strain resulting from the application of a unit sinusoidal stress. The storage compliance, J_1, represents the strain amplitude that is in phase with the driving stress. The loss compliance, J_2, is the component that is $\frac{\pi}{2}$ out of phase and results in dissipation. These terms are given by

$$J_1(\tau'_S) = J_U\left(1 + \frac{A_B(\tau'_S)^{\alpha_B}}{\alpha_B} + \frac{\sqrt{2\pi}}{2}A_P\,\sigma_P\left\{1 - \mathrm{erf}\left[\frac{\ln(\tau'_P/\tau'_S)}{\sqrt{2}\sigma_P}\right]\right\}\right) \tag{4}$$

and

$$J_2(\tau'_S) = J_U\frac{\pi}{2}\left\{A_B(\tau'_S)^{\alpha_B} + A_P\,\exp\left[\frac{-\ln^2(\tau'_P/\tau'_S)}{2\sigma_P^2}\right]\right\} + J_U\tau'_S \tag{5}$$

where $A_B = 0.664$ and $\alpha_B = 0.38$ represent the amplitude and slope of high-temperature background stress relaxation and J_U is the unrelaxed compliance. A_P and σ_P represent the amplitude and width of a high frequency relaxation peak superimposed upon this background trend such that

$$A_P(T') = \begin{cases} 0.01 & \text{for } T' < 0.91 \\ 0.01 + 0.4(T' - 0.91) & \text{for } 0.91 \leq T' < 0.96 \\ 0.03 & \text{for } 0.96 \leq T' < 1 \\ 0.03 + \beta(\varphi) & \text{for } T' \geq 1 \end{cases} \tag{6}$$

and

$$\sigma_P(T') = \begin{cases} 4 & \text{for } T'0.92 \\ 4 + 37.5(T' - 0.92) & \text{for } 0.92 \leq T'1 \\ 7 & \text{for } T' \geq 1 \end{cases} \tag{7}$$

where $T' = \frac{T}{T_s}$ is the homologous temperature, T is the temperature, and T_s is the solidus (i.e., melting) temperature, both in Kelvin. φ is the melt fraction and $\beta(\varphi)$ describes the direct poroelastic effect of melt, which is assumed to be unimportant within the upper mantle where only very low volumes of melt are

expected to be retained (e.g., ~0.1%; McKenzie, 2000; Takei, 2017). J_U is the inverse of the unrelaxed shear modulus, $\mu_U(P,T)$, such that

$$J_U(P,T)^{-1} = \mu_U(P,T) = \mu_0 + \frac{\partial \mu}{\partial T}(T - T_0) + \frac{\partial \mu}{\partial P}(P - P_0) \tag{8}$$

where μ_0 is the unrelaxed shear modulus at surface pressure-temperature conditions (i.e., $P = P_0$, $T = T_0$), the differential terms are assumed to be constant, and the pressure, P, in GPa is linearly related to the depth, z, in km by $\frac{z}{30}$. The normalized shear wave period, τ_S', in Equations 4 and 5 is equal to $\frac{\tau_S}{2\pi\tau_M}$, where τ_S is the shear wave period and $\tau_M = \frac{\eta}{\mu_U}$ is the normalized Maxwell relaxation timescale. Using $\tau_S = \frac{z}{1.4}$ takes into account changes in the Rayleigh wave period that is most sensitive to ambient velocity structure as a function of depth (Forsyth, 1992). τ_P' represents the normalized shear wave period associated with the center of the high frequency relaxation peak, which was found to be 6×10^{-5}. The steady-state diffusion creep viscosity, η, is given by

$$\eta = \eta_r \left(\frac{d}{d_r}\right)^m \exp\left[\frac{E_a}{R}\left(\frac{1}{T} - \frac{1}{T_r}\right)\right] \exp\left[\frac{V_a}{R}\left(\frac{P}{T} - \frac{P_r}{T_r}\right)\right] A_\eta \tag{9}$$

where d is grain size, m is the grain size exponent, R is the gas constant, E_a is the activation energy, and V_a is the activation volume. The subscript r refers to reference values within the upper mantle, which are assumed to be $d_r = d = 1$ mm, $P_r = 1.5$ GPa and $T_r = 1200$°C. A_η represents the extra reduction of viscosity caused by an increase in E_a close to the solidus, which is given by

$$A_\eta(T') = \begin{cases} 1 & \text{for } T' < T_\eta' \\ \exp\left[-\frac{(T' - T_\eta')}{T'(1 - T_\eta')}\ln(\gamma)\right] & \text{for } T_\eta' \le T' < 1 \\ \gamma^{-1}\exp(-\lambda\varphi) & \text{for } T' \ge 1. \end{cases} \tag{10}$$

where $T_\eta' = 0.94$ is the homologous temperature above which the effective activation energy increases beyond its original value, and $\gamma = 5$ is the factor of additional viscosity reduction. The term $\lambda\varphi$ describes the direct effect of melt on viscosity, which is assumed to be negligible at low melt volumes. The solidus temperature, T_s, is fixed to a value of 1326°C at 50 km, equivalent to a dry peridotite solidus (Hirschmann, 2000). It linearly increases below this depth in accordance with

$$T_s(z) = 1599 + \frac{\partial T_s}{\partial z}(z - 50) \tag{11}$$

where $\frac{\partial T_s}{\partial z}$ is the gradient of the solidus. We assume a temperature-dependent and compressible density, $\rho(P,T)$, following the approach of Grose and Afonso (2013). First, we define a linear temperature dependence for thermal expansivity, $\alpha(T)$, such that

$$\alpha(T) = \alpha_0 + \alpha_1 T \tag{12}$$

where $\alpha_0 = 2.832 \times 10^{-5}\,\mathrm{K}^{-1}$ and $\alpha_1 = 0.758 \times 10^{-8}\,\mathrm{K}^{-2}$ are constants calibrated by mineral physics experiments (Bouhifd et al., 1996). In order to include pressure dependence, the isothermal volume change, $(V_0/V)_T$, is calculated at each pressure using the Brent minimization algorithm and the third-order Birch-Murnaghan equation of state given by

$$P = \frac{3}{2}K_0\left[\left(\frac{V_0}{V}\right)_T^{\frac{7}{3}} - \left(\frac{V_0}{V}\right)_T^{\frac{5}{3}}\right]\left\{1 + \frac{3}{4}(K_T' - 4)\left[\left(\frac{V_0}{V}\right)_T^{\frac{2}{3}} - 1\right]\right\} \tag{13}$$

where $K_0 = 130$ GPa is the bulk modulus at zero pressure and $K_T' = 4.8$ is the pressure derivative of the isothermal bulk modulus. The associated isothermal density change with pressure, $\rho(P)$, is given by

$$\rho(P) = \rho_0 \left(\frac{V_0}{V}\right)_T \tag{14}$$

where $\rho_0 = 3{,}330\ \mathrm{kg\ m^{-3}}$ is the density of mantle at surface pressure and temperature. The effect of pressure on thermal expansivity is included by using

$$\frac{\alpha(P,\ T)}{\alpha(T)} = \left(\frac{V_0}{V}\right)_T \exp\left\{(\delta_T + 1)\left[\left(\frac{V_0}{V}\right)_T^{-1} - 1\right]\right\} \tag{15}$$

where $\delta_T = 6$ is the Anderson-Grüneisen parameter. Thus, density as a function of both pressure and temperature, $\rho(P,T)$, can be calculated using

$$\rho(P,\ T) = \rho_0 \left(\frac{V_0}{V}\right)_T \left\{1 - \left[\frac{\alpha(P,\ T)}{\alpha(T)}\right]\left[\alpha_0(T - T_0) + \frac{\alpha_1}{2}\left(T^2 - T_0^2\right)\right]\right\} \tag{16}$$

where $T_0 = 273\ \mathrm{K}$ is temperature at the surface. In an analogous fashion to Equation 3, the shear wave attenuation, Q_S^{-1}, is defined as

$$Q_S^{-1} = \frac{J_2}{J_1}\left[\frac{1 + \sqrt{1 + (J_2/J_1)^2}}{2}\right]^{-1} \simeq \frac{J_2}{J_1} \tag{17}$$

4.2. Model Calibration

Parameters that control the dependence of anelasticity upon frequency and homologous temperature (i.e., A_B, α_B, τ'_P, $\beta(\varphi)$, γ, T'_η, and $\lambda\varphi$) are directly constrained by forced oscillation experiments on borneol (Yamauchi & Takei, 2016). However, μ_0, $\frac{\partial\mu}{\partial T}$, $\frac{\partial\mu}{\partial P}$, η_r, E_a, V_a, and $\frac{\partial T_s}{\partial z}$ are material properties that depend upon mantle mineralogy and must be independently determined.

A common approach is to assume a mantle composition and model the anharmonic velocity (i.e., the elastic component) as a function of temperature and pressure by calculating values of μ_0, $\frac{\partial\mu}{\partial T}$, and $\frac{\partial\mu}{\partial P}$ using a Gibbs free energy minimization algorithm coupled with relevant thermodynamic databases of mineral properties (Connolly, 2009; Cottaar et al., 2014; Stixrude & Lithgow-Bertelloni, 2005, 2011). A correction for anelastic effects can then be calculated using rheological parameters and solidus gradients that are determined from laboratory experiments on mantle minerals (i.e., η_r, E_a, V_a, and $\frac{\partial T_s}{\partial z}$). In this way, V_S is converted into temperature via a forward modeling approach (Cammarano et al., 2009; Dannberg et al., 2017; Goes et al., 2012; Karato, 1993).

Although this approach is widely applied to seismic tomographic models, it has several limitations. For example, there are uncertainties in mantle composition, in grain size, and in the rheological process that is responsible for anelastic deformation. There are also significant discrepancies in velocity structure imaged by different tomographic models that arise from variations in regularization, in model parameterization, and in reference model choices. Consequently, even when a consistent set of material parameters are used, considerable differences in inferred density structure are obtained from different tomographic models (Priestley & McKenzie, 2013).

Here, we adopt an alternative approach that was pioneered by Priestley and McKenzie (2006, 2013). It exploits the fact that, although seismic velocities vary due to tomographic inversion choices, and mantle grain size and composition remain uncertain, there are a range of average mantle properties for which independent constraints do exist. These constraints include the evolving thermal structure of cooling oceanic lithosphere, locally determined geothermal profiles within continental lithosphere, and the adiabatic temperature gradient of convecting mantle. Any model of thermal structure obtained by analyzing tomographic models should be as consistent as possible with these independent constraints. Agreement can be achieved using the anelastic parameterization to invert for a suite of material property values that minimize the misfit

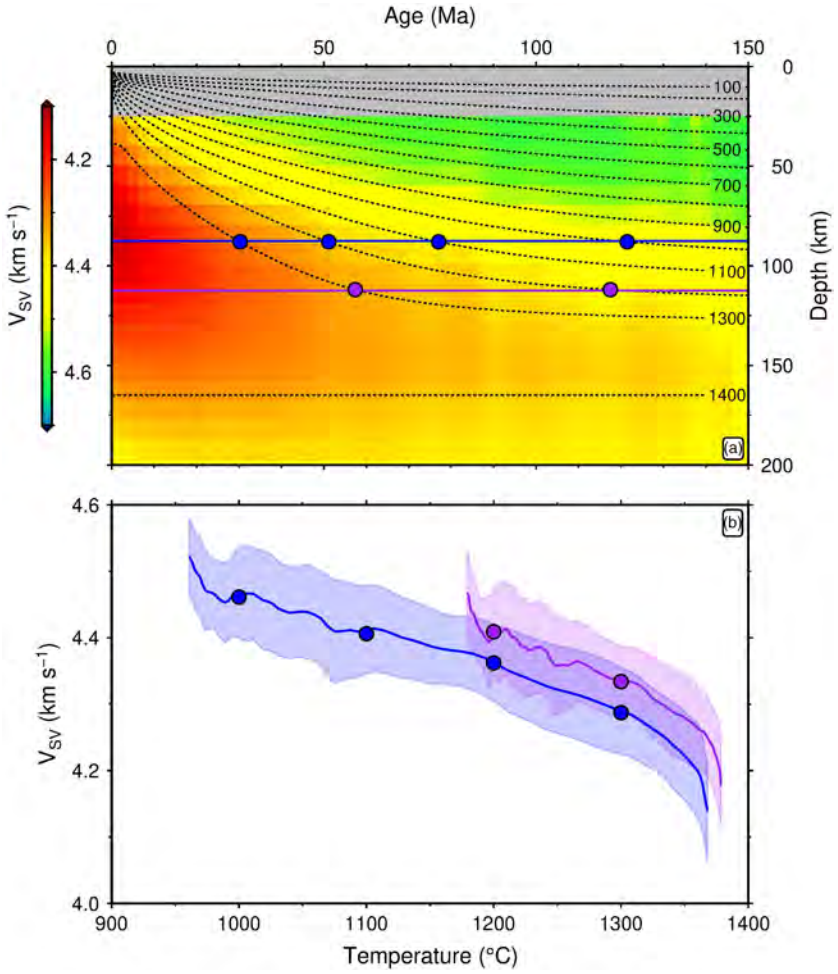

Figure 5. Shear wave velocity as a function of temperature and pressure. (a) Vertical slice through global stack of V_{SV} as a function of age and depth for SL2013sv model (Schaeffer & Lebedev, 2013). Numbered black dashed lines = isothermal surfaces from plate cooling model labeled according to temperature in °C (Richards et al., 2018); horizontal blue and purple lines = depths of 87.5 km and 112.5 km, respectively; colored circles = intersections between this depth slice and isothermal surfaces. (b) V_{SV} plotted as a function of temperature for each depth window. Blue and purple lines = extracted relationships between V_{SV} and temperature at depths of 87.5±12.5 km and 112.5±12.5 km, respectively; colored bands = $\pm 1\sigma$ uncertainty calculated from global stack; colored circles = intersections shown in panel (a).

between observed and calculated temperature, attenuation and viscosity. One advantage of this inverse strategy is that, by individually calibrating different tomographic models, more consistent and realistic predictions of upper mantle temperature and density can be obtained whose uncertainties can be quantitatively determined.

4.2.1. Independent Constraints

To determine optimal material property values for the anelastic parameterization, we generate four sets of observational constraints that help to determine shear wave velocity, attenuation and viscosity as a function of temperature and pressure within the upper 400 km of the oceanic mantle, where olivine is the dominant mineral phase. These constraints are selected to cover a broad range of temperature and pressure conditions. The anelastic parameterization is then inverted to minimize misfit to the observational constraints, yielding a self-consistent suite of thermomechanical properties at other locations throughout the oceanic realm.

The first constraint is the well-established relationship between temperature and shear wave velocity as a function of age and depth for the portion of oceanic upper mantle that is cooling by conduction (Ritzwoller et al., 2004). This empirical relationship is constructed by combining the globally averaged shear wave velocity stack of a given tomographic model with the thermal structure predicted for a cooling plate

using an ambient potential temperature of 1333°C and an equilibrium plate thickness of 133 km (Richards et al., 2018). Note that several tomographic models provide isotropic shear wave velocities, V_S, while other models only give the vertically polarized component, V_{SV}. Either value can be used in our inverse strategy since calibrating the anelastic parameterization provides a self-consistent conversion into temperature that circumvents the need to assume an *a priori* radial anisotropic profile (Ma et al., 2020).

Since tomographic models have a vertical resolution of tens of kilometers, we extract a series of velocity-temperature pairs by using the average value of V_S between 75 km and 100 km and the temperature obtained from the plate model at a midpoint depth of 87.5 km (Figure 5). A set of deeper points is extracted by using the 100 km and 125 km depth slices. We do not analyze the 25 km depth slice since it is susceptible to artifacts introduced by downward bleeding of crustal velocities. We also exclude the 50 km depth slice for two reasons. First, there is a relatively strong correlation between spreading rate and V_S at a depth of 50 km beneath mid-ocean ridges (supporting information Figure S1). Dalton et al. (2014) suggest that this relationship is an artifact of the limited horizontal resolution of tomographic models, which results in aliasing of temperature-induced lateral velocity variations beneath the narrower, slow-spreading ridges. Second, compositional changes related to the depth of the garnet-spinel transition together with depletion during melt extraction at the ridge could have a non-negligible impact on V_S values at this depth, which would complicate our calibration strategy (Ma & Dalton, 2019). The misfit, H_1, between observed and calculated values of V_S is determined using

$$H_1 = \sqrt{\frac{1}{N_1}\sum_{i=1}^{N_1}\frac{1}{M}\sum_{j=1}^{M}\left(\frac{V_{ij}^o - V_{ij}^c}{\sigma_{ij}}\right)^2} \tag{18}$$

where V_{ij}^o are average values of observed shear wave velocities within each depth window, σ_{ij} is the average standard deviation obtained from the global stack, and V_{ij}^c are the average velocities calculated using Equation 3. $M = 76$ is the number of age bins and $N_1 = 2$ is the number of depth windows.

The second constraint concerns the temperature gradient within the convecting interior of the mantle, which is expected to follow an isentropic gradient. At these depths, the globally averaged value of V_S should reflect this temperature condition. We therefore take the mean values of V_S between 225 km and 400 km depth beneath the oceans and combine them with temperatures for a 1333°C isentrope, calculated using the parameterization of Shorttle et al. (2014). This formulation is adopted to ensure consistency with the temperature profile at the ridge axis implemented by the plate model of Richards et al. (2018) and yields an average crustal thickness of ~7 km during decompression melting of an aluminous lherzolite source (Katz et al., 2003; White et al., 1992). The 225–400 km depth range is chosen for two reasons. First, it is located well below any non-adiabatic complications associated with the thermal boundary layer. Second, tomographic models that are constructed primarily from surface waves have limited resolving power at greater depths. The misfit, H_2, between observed and calculated values of V_S is given by

$$H_2 = \sqrt{\frac{1}{N_2}\sum_{i=1}^{N_2}\left(\frac{V_i^o - V_i^c}{\sigma_i}\right)^2} \tag{19}$$

where $N_2 = 8$ is the number of depth slices between 225 km and 400 km.

A third constraint comes from the seismic attenuation properties of oceanic mantle, which is related to the anelastic parameterization through Equation 17. It has been observed that V_S and Q_S^{-1} in the upper mantle systematically covary for oceanic lithosphere $\geq$ 100 Ma (Adenis et al., 2017; Dalton et al., 2009). Here, we determine the radial variation of Q_S^{-1} between 150 km and 400 km depth by averaging attenuation values from the QRFSI12 model of Dalton et al. (2009) beneath oceanic lithosphere older than 100 Ma. Since temperature conditions in the shallow asthenosphere do not necessarily follow an adiabatic gradient, Q_S^{-1} cannot be directly pinned to an isentropic temperature but is instead tied to temperature given by the equivalently averaged V_S profile from each tomographic model. The misfit, H_3, between observed and calculated attenuation is given by

$$H_3 = \sqrt{\frac{1}{N_3}\sum_{i=1}^{N_3}\left(\frac{Q_i^{-1\,o} - Q_i^{-1\,c}}{\sigma_i}\right)^2} \tag{20}$$

where $Q_i^{-1\,o}$ and $Q_i^{-1\,c}$ are observed and calculated values of attenuation. $N_3 = 15$ is the number of depth slices between 150 km and 400 km.

One advantage of the anelastic parameterization described by Yamauchi and Takei (2016) is that η is equivalent to the diffusion creep viscosity under steady-state deformation. As a final constraint, we therefore use Equation 9 to force the average viscosity between 225 km and 400 km to approximate the value obtained by glacial isostatic adjustment analysis. Here, a bulk viscosity of $\eta_{UM} = 3 \times 10^{20}$ Pa s obtained for the upper mantle between 100 km and 670 km by Lau et al. (2016) is assumed. The misfit, H_4, between assumed and calculated viscosity is calculated using

$$H_4 = \sqrt{\frac{1}{\log_{10}(\sigma_i)^2}\left\{\left[\frac{1}{N_4}\sum_{i=1}^{N_4}\log_{10}(\eta_i^c)\right] - \log_{10}(\eta_{UM})\right\}^2} \tag{21}$$

where η_i^c are calculated values of viscosity and $N_4 = 8$ is the number of depth slices between 225 km and 400 km. We assume that the bulk viscosity uncertainty, σ_i, is 1 order of magnitude.

Despite the longer timescale of deformation over glacial cycles compared with seismic wave propagation, we suggest that this rheological constraint is justifiable for two reasons. First, the glacial isostatic adjustment models that independently constrain the value of η_{UM} implicitly assume linear viscoelasticity (i.e., a linear relationship between stress and strain; Lambeck et al., 1998). Second, over the depth range of interest, diffusion creep is thought to dominate over dislocation creep, based upon a combination of observational evidence for the depth dependence of seismic anisotropy and the extrapolation of experimentally calibrated creep laws to upper mantle conditions (Karato & Wu, 1993). Nevertheless, we acknowledge that the Maxwell frequency scaling that underpins the anelastic parameterization, together with its applicability to long-term inferences about viscosity, remains a controversial topic (e.g., Faul & Jackson, 2015; Lau & Holtzman, 2019). Consequently, we have also tested the effect of omitting this constraint from our inversion procedure. This test results in similar optimal values for material properties, although the associated parameter uncertainties are greater.

The four individual misfit functions are combined into a single cost function, H_w, such that

$$H_w = \frac{\sum_{i=1}^{n} w_i H_i}{\sum_{i=1}^{n} w_i} \tag{22}$$

where w_i are weighting coefficients that are applied to each constraint. In contrast to previous studies, we have avoided including thermobarometric constraints derived from continental garnet peridotite xenoliths (cf. Priestley & McKenzie, 2006, 2013; Yamauchi & Takei, 2016). These xenolith suites sample regions with thick and generally depleted continental lithosphere, where the potential effects of compositional variations on both the anharmonic and anelastic components of V_S are not well known. In addition, these xenolith constraints yield estimates of the palaeogeothermal gradient at the time of their eruption, which may differ from present-day gradients. Since our primary objective is to obtain an accurate V_S-to-density parameterization for fertile oceanic mantle, we have chosen to omit these separate continental constraints. Nevertheless, it has been shown that continental geotherms calculated using our ocean-only approach provide a good match to Australian paleogeotherms that in some cases are over a billion years old (Hoggard et al., 2020b).

4.2.2. Inverse Optimization

The weighted misfit function, H_w, is minimized in two steps. First, parameter sweeps are carried out to identify the approximate location of the global minimum. During these sweeps, μ_0 is varied between 69 and 82 GPa in increments of 1 GPa, $\frac{\partial \mu}{\partial T}$ between −24 and −8 MPa °C^{-1} in increments of 2 MPa °C^{-1}, $\frac{\partial \mu}{\partial P}$ between 1.5 and 2.9 in increments of 0.2, η_r between 10^{17} and 10^{23} Pa s in increments of $10^{0.5}$ Pa s, E_a between 100 and 1,000 kJ mol^{-1} in increments of 100 kJ mol^{-1}, V_a between 0 and 30 cm^3 mol^{-1} in increments of 2 cm^3

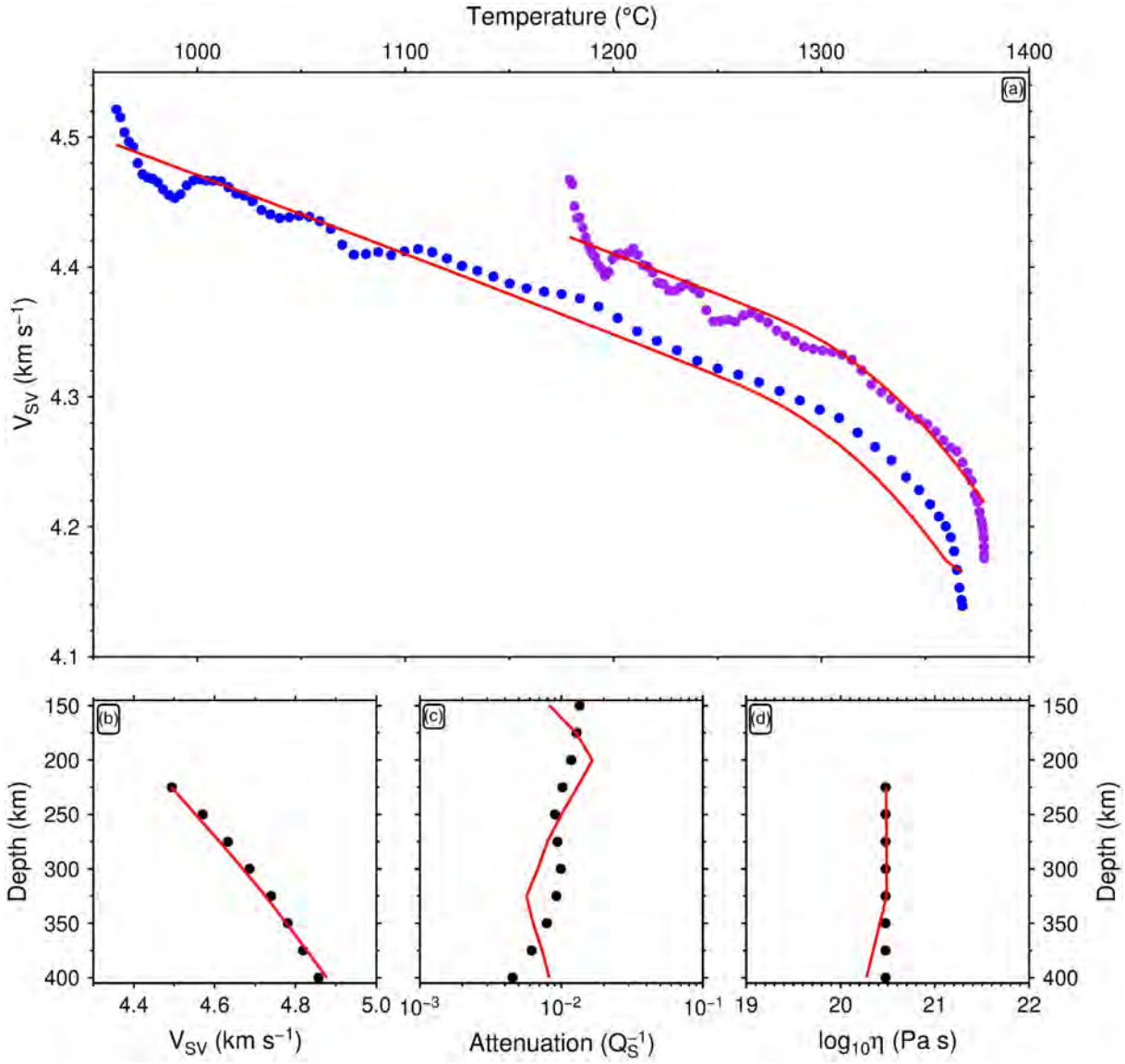

Figure 6. Calibration of anelastic parameterization for SL2013sv model. (a) V_{SV} plotted as a function of temperature for plate model. Blue and purple circles = pairs of average V_{SV} and temperature values at depths of 87.5 km and 112.5 km, respectively (Figure 5b); red lines = best-fit relationships obtained by inverse modeling of anelastic parameterization. (b) V_{SV} plotted as a function of depth for convecting mantle interior. Black circles = average values of V_{SV}, where temperature is assumed to track the 1333°C isentrope; red line as before. (c) Attenuation, Q_S^{-1}, plotted as a function of depth. Black circles = average values of Q_S^{-1} beneath oceanic lithosphere that is >100 Ma extracted from QRFS12 model of Dalton et al. (2009); red line as before. (d) Steady-state diffusion creep viscosity, η, plotted as a function of depth. Black circles = bulk upper mantle value of 3×10^{20} Pa s determined by glacial isostatic adjustment study of Lau et al. (2016); red line as before.

mol^{-1}, and finally $\frac{\partial T_s}{\partial z}$ between 0 and 4.5°C km^{-1} in increments of 0.25°C km^{-1}. These ranges are chosen to exceed the extremal range of values constrained by mineral physics experiments and by existing anelastic parameterizations, in order to ensure that the optimization procedure is not preconditioned to only reproduce the results of pre-existing studies (Cammarano et al., 2003; Hirth & Kohlstedt, 2003; Isaak, 1992; Jain et al., 2018; Karato, 2010; Kohlstedt et al., 1995; Mao et al., 2015; Priestley & McKenzie, 2013; Takei, 2017; Thomson et al., 2016; Yamauchi & Takei, 2016). Second, Powell's conjugate gradient algorithm is used to further minimize the value of H_w by taking best-fitting parameter values obtained from the parameter sweep as an initial solution (Press et al., 1992). For this minimization, we set $w_1 = 10$, $w_2 = 1$, $w_3 = 2$ and $w_4 = 2$. Note that each of these coefficients can vary by up to 1 order of magnitude

without materially affecting our results. Optimization yields a minimum misfit of $H_w = 0.463$ located at $\mu_0 = 78.2 \pm 2.2$ GPa, $\frac{\partial \mu}{\partial T} = -20.0 \pm 1.9$ MPa °C^{-1}, $\frac{\partial \mu}{\partial P} = 2.67 \pm 0.18$, $\log_{10}\eta_r = 22.6 \pm 1.6$ Pa s, $E_a = 400 \pm 288$ kJ mol^{-1}, $V_a = 0.092 \pm 5.560$ cm^3 mol^{-1}, and $\frac{\partial T_s}{\partial z} = 0.919 \pm 0.257$°C km^{-1}. Quoted parameter uncertainties have been constructed using the diagonal components of the *a posteriori* covariance matrix (section 4.2.3).

The recovered set of optimal parameter values yield adequate fits to the suite of observational constraints that are, as previously reported by Priestley and McKenzie (2013) and by Yamauchi and Takei (2016), in broad agreement with mineral physics measurements (Figure 6). The inverted value of μ_0 is in better agreement with experimental constraints than the results of previous studies (Cammarano et al., 2003; Isaak, 1992). However, values of $\frac{\partial \mu}{\partial T}$ and $\frac{\partial \mu}{\partial P}$ are higher than the experimental values of approximately -14 MPa °C^{-1} and 1.8, respectively (Isaak, 1992; Mao et al., 2015).

Some of this discrepancy may result from our use of vertically polarized shear wave velocities in our input constraints, whereas mineral physics experiments generally assume isotropic shear modulus properties. The inverted solidus gradient of ~1°C km^{-1} is significantly lower than the value of ~4°C km^{-1} that is expected for dry peridotite (Katz et al., 2003). We note that the presence of minor quantities of CO_2 and water within the upper mantle is more consistent with this gradient and has also been invoked to account for high attenuation values in the asthenosphere (Eilon & Abers, 2017; Thomson et al., 2016). The recovered value of the activation energy is 400±273 kJ mol^{-1}, which is toward the upper limit of the range of experimental values expected for diffusion creep (i.e., 240–425 kJ mol^{-1}; Fei et al., 2012; Hirth & Kohlstedt, 2003; Karato & Wu, 1993). Finally, the value of activation volume is 0.1±5.7 cm^3 mol^{-1}, which overlaps with the lower bound obtained for diffusion creep (i.e., 0–10 cm^3 mol^{-1}), although the value of this parameter is poorly constrained by rock deformation experiments (Hirth & Kohlstedt, 2003; Jain et al., 2018).

4.2.3. Uncertainties and Trade-Offs

Our two-step optimization procedure was designed to help reduce the possibility of converging on local minima of the misfit function. Assuming that we have correctly located the global minimum, it is useful to examine the trade-off between the seven material parameter values. Here, two complementary approaches have been implemented. First, the cost function, H_w, is evaluated for sweeps of all individual pairs of parameter values, keeping the five others fixed (Figure 7). Second, parameter trade-off is more formally analyzed by calculating the Hessian matrix of the cost function, $\mathbf{Hess}(H_w)$. The required second and cross derivatives at the global minimum are numerically calculated using a centered finite-difference approximation (see Equation (9) of Ridout, 2009). When constructing the Hessian matrix, best-fitting parameter values, p^i, are normalized using $p^i_n = \frac{p^i - p^i_{min}}{p^i_{max} - p^i_{min}}$ to ensure similar magnitudes of variation. p^i_n is the normalized value between 0 and 1, p^i_{min} is the minimum parameter value recovered in the initial parameter sweep, and p^i_{max} is the corresponding maximum value. A step size of 0.02 was used in the finite-difference scheme, which helps to minimize rounding and truncation errors.

The covariance matrix, which provides directions of linear relationships between different parameter values, is given by

$$\mathbf{Cov}(H_w) = 2\chi^2_\nu [\mathbf{Hess}(H_w)]^{-1} \tag{23}$$

where χ^2_ν represents the reduced chi-square statistic (the chi-square misfit between observed and predicted values normalized by the number of degrees of freedom of the cost function, i.e., the number of data points minus the seven fitted parameters). The correlation matrix, which provides information about the strength of parameter trade-offs, is given by

$$\mathbf{Corr}(H_w) = \{\mathrm{diag}[\mathbf{Cov}(H_w)]\}^{-\frac{1}{2}} \mathbf{Cov}(H_w) \{\mathrm{diag}[\mathbf{Cov}(H_w)]\}^{-\frac{1}{2}} \tag{24}$$

This matrix yields values that range between +1 and −1, corresponding to the strength of positive and negative linear correlations between different parameter pairs (Figure 8).

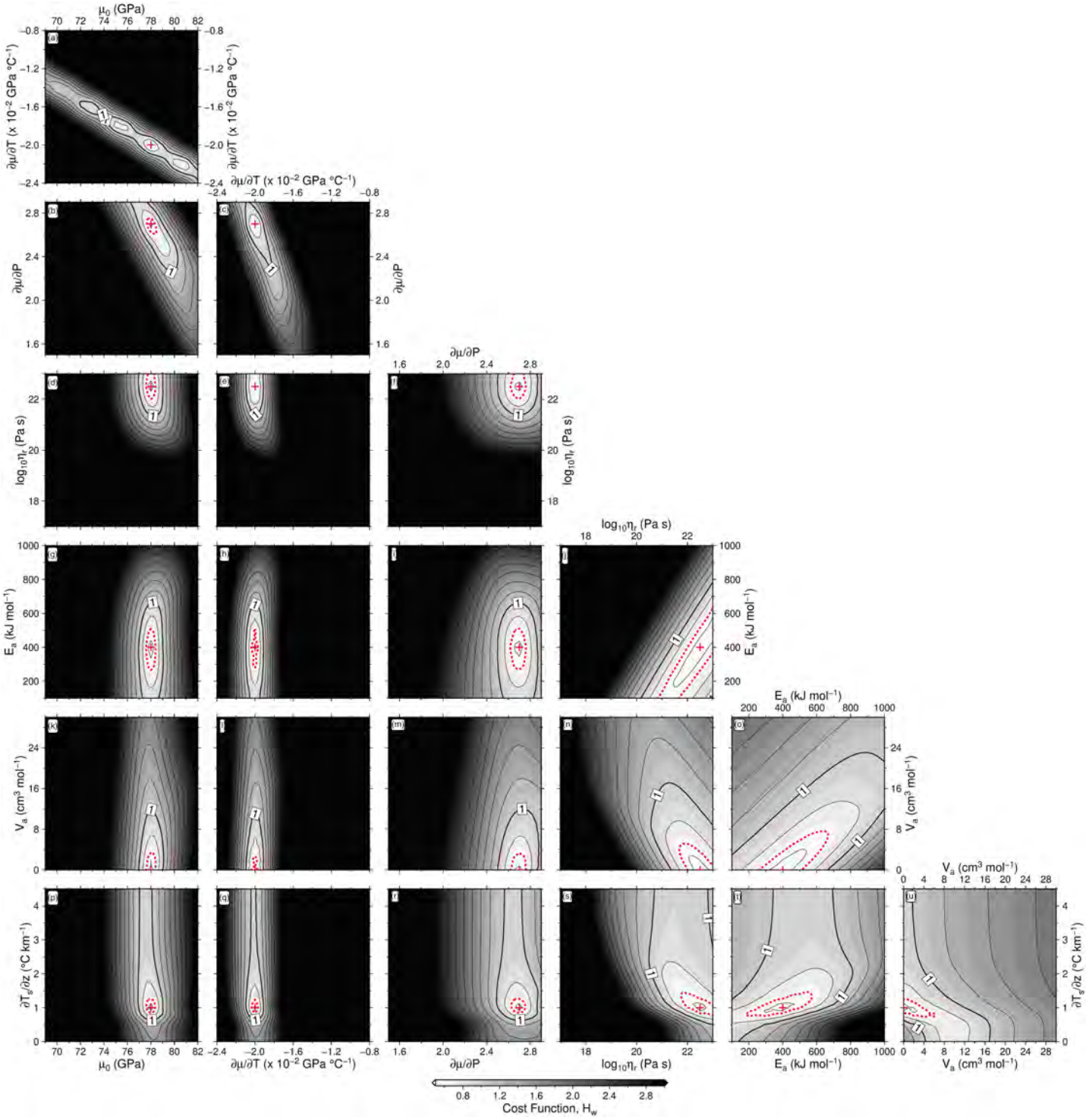

Figure 7. Contour plots of cost function. (a) Misfit, H_w, as a function of μ_0 and $\frac{\partial \mu}{\partial T}$. Red cross = global minimum; red dotted line = contour line showing 125% of value at global minimum (this contour line is omitted if it overlaps with the red cross). (b) Same as a function of μ_0 and $\frac{\partial \mu}{\partial P}$. (c) $\frac{\partial \mu}{\partial T}$ and $\frac{\partial \mu}{\partial P}$. (d) μ_0 and η_r. (e) $\frac{\partial \mu}{\partial T}$ and η_r. (f) $\frac{\partial \mu}{\partial P}$ and η_r. (g) μ_0 and E_a. (h) $\frac{\partial \mu}{\partial T}$ and E_a. (i) $\frac{\partial \mu}{\partial P}$ and E_a. (j) η_r and E_a. (k) μ_0 and V_a. (l) $\frac{\partial \mu}{\partial T}$ and V_a. (m) $\frac{\partial \mu}{\partial P}$ and V_a. (n) η_r and V_a. (o) E_a and V_a. (p) μ_0 and $\frac{\partial T_s}{\partial z}$. (q) $\frac{\partial \mu}{\partial T}$ and $\frac{\partial T_s}{\partial z}$. (r) $\frac{\partial \mu}{\partial P}$ and $\frac{\partial T_s}{\partial z}$. (s) η_r and $\frac{\partial T_s}{\partial z}$. (t) E_a and $\frac{\partial T_s}{\partial z}$. (u) V_a and $\frac{\partial T_s}{\partial z}$.

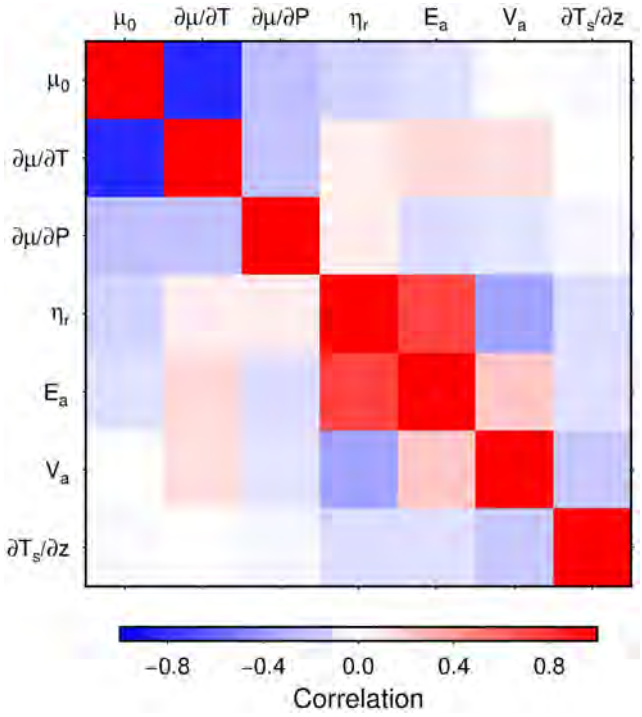

Figure 8. Correlation matrix. Colored squares indicate degree of linear correlation between each pair of parameter values in vicinity of global minimum.

These approaches show that there are two principal groups of trade-off (Figures 7 and 8). The first group involves μ_0, $\frac{\partial \mu}{\partial T}$, and $\frac{\partial \mu}{\partial P}$, which together control the anharmonic velocity. The second group involves η_r, E_a, V_a, and $\frac{\partial T_s}{\partial z}$, which together control the onset and magnitude of anelastic effects. Covarying parameter values along these trade-off relationships has only a limited impact on misfit, which accounts for the fact that the inverse algorithm returns a range of likely parameter values. The misfit well is particularly shallow for E_a and V_a, with values that vary from 200 to 600 kJ mol^{-1} and from 0 to 8 cm^3 mol^{-1}, respectively. These parameter values clearly trade off strongly against each other, and individually they are poorly constrained. Nevertheless, these ranges of uncertainty are consistent with experimentally determined constraints according to a Bayesian analysis of rock deformation measurements (Jain et al., 2018). Importantly, calibration of parameters against independent temperature estimates yields information about the strength and orientation of any trade-offs. Thus, while individual parameter uncertainty can still be large, exploiting this covariance can reduce the uncertainty of inferred upper mantle temperature structure in comparison with forward modeling strategies.

5. Testing Temperature Predictions

Having calibrated appropriate material parameter values, the validity of the calculated upper mantle thermal structure can be tested against independent estimates. For example, average asthenospheric temperatures between 75 km and 200 km beneath ridge axes have a global range of ±125°C, which agrees with estimates based upon geochemical analyses of mid-ocean ridge basalts (MORB; Dalton et al., 2014; Herzberg et al., 2007). Axial crustal thickness measurements also provide a useful test since the total melt fraction generated by adiabatic decompression melting is strongly dependent upon the potential temperature of upwelling asthenosphere (Shorttle et al., 2014). Here, observations from oceanic lithosphere that is younger than 5 Ma and within 300 km of ridge axes are extracted from the global compilation of Hoggard et al. (2017) and averaged over each ridge segment from the database of Gale et al. (2014). The resultant data set of 42 measurements correlate well with present-day asthenospheric temperature anomalies calculated using the calibrated SL2013sv model, which have approximately ±60°C uncertainties ($r = 0.74$;

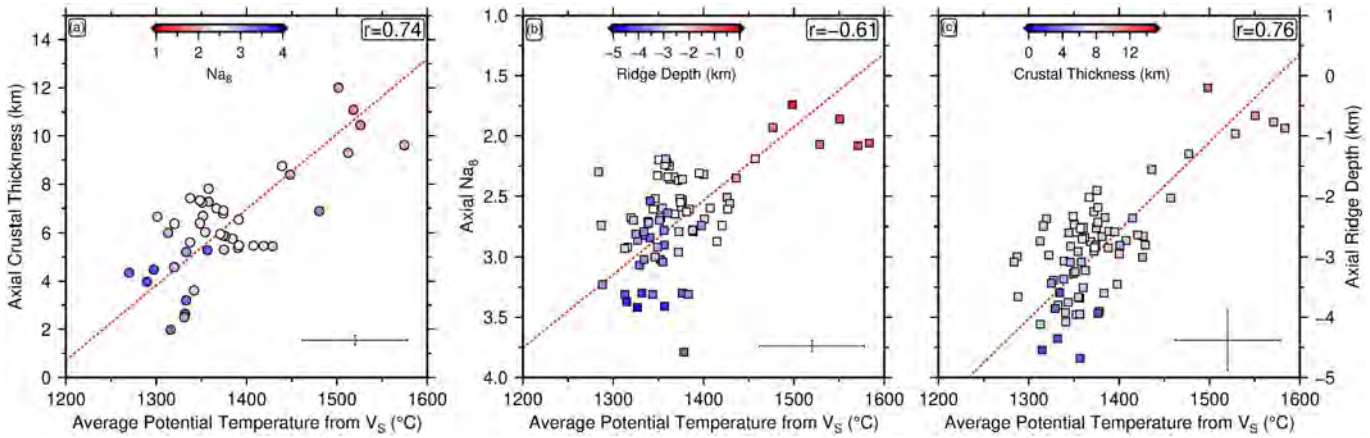

Figure 9. Independent tests of V_S-derived potential temperatures. (a) Axial crustal thickness measurements plotted as a function of average potential temperature between 75 km and 200 km, calculated from SL2013sv model. Circles = average crustal thickness measurements (colored according to Na_8 value) for oceanic lithosphere that is younger than 5 Ma and located within 300 km of ridge axis (Hoggard et al., 2017). Measurements are averaged for each ridge segment from database of Gale et al. (2013). r = Pearson's correlation coefficient; error bars at bottom right-hand corner = representative uncertainties. Note that temperature uncertainty is estimated by repeating anelastic calibration for $\pm 1\sigma$ bounds of input constraints. (b) Same for axial values of Na_8. Squares = average values per ridge segment with more than 30 dredge sample analyses, colored according to axial ridge depth (Gale et al., 2014). (c) Same for axial ridge depths at ridge segments identical to those shown in panel (b) and colored according to axial crustal thickness. Gray points are located >200 km from nearest crustal thickness measurement.

Figure 9a). These uncertainties have been estimated by repeating the anelasticity calibration procedure using 1σ upper and lower bounds on each of the input constraints. The correlation is also encouraging given that any potential complications arising from source composition variability, the melt extraction process, and temporal changes in sub-plate temperature have been neglected.

Calculated temperatures can also be directly compared with geochemical proxies. For example, Na is relatively incompatible during melting and occurs in higher quantities in low melt fraction igneous rocks, steadily reducing in concentration as melt fraction increases. Na_8, which is defined as the expected concentration of Na_2O having corrected for fractional crystallization of olivine by extrapolating measured values of MgO back to 8 wt.%, is therefore a widely used proxy for MORB source temperature (Klein & Langmuir, 1987). At mid-ocean ridges, we observe a negative correlation between Na_8 and predicted temperature ($r = -0.61$; Figure 9b). Finally, there is a positive correlation between axial ridge depth and temperature ($r = 0.76$; Figure 9c). The relationship between Na_8 and axial ridge depth, previously documented by Gale et al. (2014), confirms that asthenospheric temperature anomalies are the dominant control on melt generation and residual depth along the global mid-ocean ridge system. The potential temperature estimates of Dalton et al. (2014) are calculated from a combination of shear wave velocity anomalies and axial ridge depths, and are therefore not truly independent. Nevertheless, we note that our temperature predictions are broadly consistent with theirs ($r \sim 0.6$; supporting information Figure S2).

6. Relationship Between Residual Depth and Mantle Density Structure

The agreement between predicted and estimated temperature perturbations at mid-ocean ridges leads us to investigate the extent to which our revised shallow mantle density structure can account for the discrepancy between observed and predicted short-wavelength dynamic topography. There are two principal factors responsible for the normal stresses that support surface deflections—isostatic contributions arising from lateral gradients of density and dynamic stresses caused by the fact that these buoyancy variations drive viscous flow (Molnar et al., 2015). Increasingly, evidence from studies of post-seismic rebound, glacial isostatic adjustment, seismic anisotropy, rapid plate motion changes, and convection simulations suggests that asthenospheric viscosities are low (i.e., 10^{19}–10^{20} Pa s; Dannberg et al., 2017; Iaffaldano & Lambeck, 2014; Lin et al., 2016; Phipps Morgan et al., 1995; van der Wal et al., 2015). Away from sinking slabs and upwelling plume conduits, lateral flow is expected to occur within this layer. Under these circumstances, the topographic contribution of normal (i.e., radial) deviatoric stresses caused by flow is minimized and dynamic

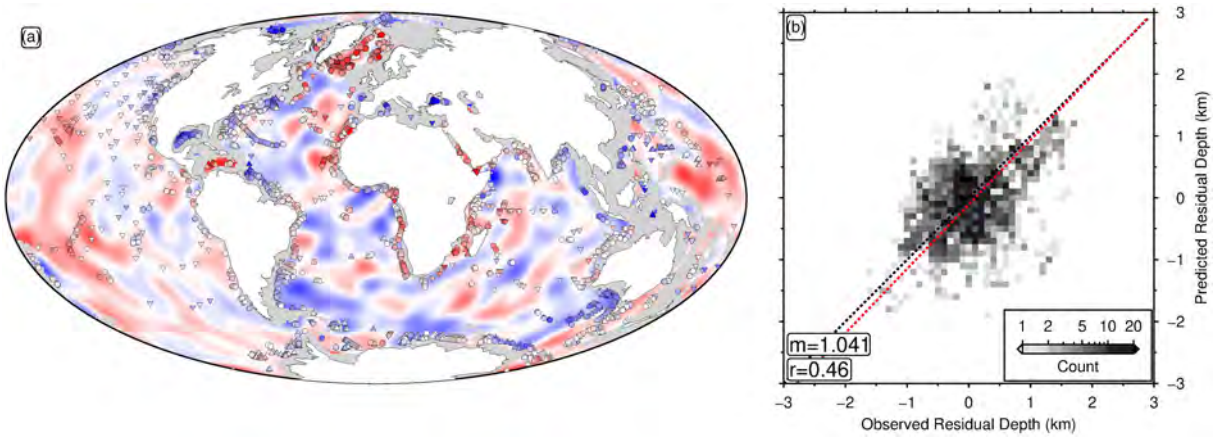

Figure 10. Global relationships between observed and predicted residual depth measurements. (a) Water-loaded residual depth calculated using SL2013sv thermal model, including contributions from lithospheric thickness changes and density anomalies within the lithosphere and asthenosphere, and assuming a compensation depth of ~240 km. Colored circles/triangles = spot measurements from Figure 1a. (b) Observed residual depth plotted against predicted residual depth at sites of spot measurements. Black dotted line = 1:1 relationship; red dotted line = best-fit linear relationship with slope, $m = 1.04$, and Pearson's correlation coefficient, $r = 0.46$.

pressure gradient forces are directed approximately parallel to the base of the lithosphere (Höink et al., 2011; Robinson et al., 1987; Semple & Lenardic, 2018). Surface deflections, δa, generated by lithospheric and asthenospheric temperature anomalies can therefore be approximated using a simple isostatic balance, whereby density anomalies are compensated at the base of the asthenosphere such that

$$\delta a = \frac{1}{\rho_b - \rho_w} \int_{z_0}^{z_b} -\Delta\rho(z,\, T,\, t)\, \mathrm{d}z \tag{25}$$

where z_0 is the upper limit of integration, which is fixed at 50 km since shallower depths appear to contain artifacts associated with downward bleeding of crustal velocities, z_b is the compensation depth, ρ_b is the mean mantle density at this depth, and $\rho_w = 1{,}030\ \mathrm{kg\,m^{-3}}$ is the density of seawater. $\Delta\rho(z,T,t)$ is the difference between the local density profile and that calculated from the global shear wave velocity stack for lithosphere of the same age, t, calculated using Equation 16. An important underpinning assumption is that lateral density changes of the lithosphere and asthenosphere are dominated by temperature variations and that compositional heterogeneity plays a secondary role. This simplification is supported by the inferred low viscosity of the asthenosphere, which likely results in it being well mixed. Furthermore, geochemical observations support this notion, since temperature has been shown to dominate upper mantle heterogeneity beneath the oceans (Dalton et al., 2014).

6.1. Global Correlations

Lithospheric and asthenospheric density anomalies inferred from the calibrated SL2013sv model have a typical peak-to-peak variation of $\pm 30\ \mathrm{kg\,m^{-3}}$. Applying Equation 25, we obtain an optimal fit between calculated and observed residual depth when z_b~240 km. This compensation depth yields maximum residual depth variations of ±2.5 km that are broadly consistent with the observational database (Figure 10a; Hoggard et al., 2017). The correlation between co-located spot measurements and predictions of residual depth is $r = 0.46$ and the best-fit linear relationship has a slope of $m = 1.04$, which is not significantly different to 1 (Figure 10b). Based on observations of the peak variation in the orientation of azimuthal anisotropy within Pacific mantle, it has been suggested that the 1200°C isothermal surface coincides with the lithosphere-asthenosphere boundary (Burgos et al., 2014; Richards et al., 2018). We calculate an average depth for this interface of ~90 km throughout the oceanic realm. The optimal compensation depth of 240 km therefore yields an average asthenospheric thickness of ~150 km.

Despite the simplicity of our isostatic approximation, our calculations that include only upper mantle density anomalies shallower than ~240 km correlate better with residual depth measurements than existing models of whole-mantle flow ($r = 0.46$; Figures 10a and 10b). The equivalent correlation coefficient for

the model of Steinberger (2007) is $r = 0.36$, which excludes contributions that are shallower than 220 km, while the model of Davies et al. (2019) includes density anomalies throughout the whole mantle and yields $r = 0.40$. Nevertheless, we acknowledge that there are regions where correlation is poor. For example, although observed and predicted residual depth anomalies are in reasonable agreement in the vicinity of the Icelandic plume, it is evident that positive residual depth measurements extend further northwest toward North America and southeast toward Scandinavia, even though the calibrated tomographic model suggests that cooler temperatures prevail. This discrepancy highlights two limitations of global tomographic models when interpreting shallow mantle structure. First, the quantity of seismograms and the proportion of each waveform that can be fitted is limited by computational expense. The resolution is further limited by geographically uneven station and event coverage. For example, in the North Atlantic Ocean, global tomographic models appear to be unable to resolve thin slow shear wave velocity anomalies that extend far from the center of the Icelandic plume, which have been resolved by regional full-waveform tomographic analysis (Rickers et al., 2013). Second, in areas of the model with poorer resolution, imaged anomalies can be smeared along ray paths (Ekström et al., 1997). This phenomenon can occur close to ocean-continent boundaries where fast shear wave velocities associated with cold, thick continental lithosphere bleeds into adjacent oceanic regions and gives rise to fast (i.e., cold) velocity artifacts, which in turn lead to negative predicted residual depth anomalies.

6.2. Regional Traverses

Spatial coverage of the global residual depth database of Hoggard et al. (2017) is inevitably uneven due to the location of modern and legacy marine seismic surveys. In general, denser coverage of spot measurements occurs adjacent to continental shelves where high-quality deep seismic reflection surveys are concentrated. Here, we present and analyze detailed transects from the margins of the South Atlantic Ocean and from the margins that surround Australia. These transects provide a useful means for assessing the ability of residual depth calculations based upon the calibrated SL2013sv model to match observed short-wavelength residual depth patterns at regional scales.

6.2.1. South Atlantic Margins

The margins of the South Atlantic Ocean are an important setting for regional comparisons due to dense data coverage and a relatively uniform age of oceanic lithosphere abutting the margins. Thus, along-strike variations in residual depth are well resolved and less affected by the choice of reference age-depth relationship (Hoggard et al., 2017). Both margins are characterized by striking quasi-sinusoidal excursions of residual depth that have wavelengths of ~1,500 km and amplitudes of ±1 km. Residual V_{SV} anomalies averaged between 75 km and 250 km show broad agreement with these spot measurement throughout the South Atlantic Ocean (Figure 11a).

Along the South American margin, the fit between observed and calculated residual depth is reasonable, although there is a significant discrepancy offshore Brazil in the vicinity of Rio Grande Rise at ~10°S (Figures 11b and 11c). There are two potential causes of this mismatch. First, it may reflect spatial bleeding of high velocities away from thick cold continental lithosphere of the adjacent São Francisco craton out into the oceanic lithosphere. Second, it could be related to a lithospheric depletion event associated with Early Cretaceous melt extraction that formed the Paraná Large Igneous Province. If present, thick and depleted lithosphere is expected to have anomalously fast velocity that could be erroneously calibrated as cold and dense material (Schutt & Lesher, 2006).

Along the West African margin, the agreement between observed and calculated residual depth is generally good (Figures 11d and 11e). Here, quasi-sinusoidal oscillations of residual depth are particularly well developed between Equatorial Guinea at 5°N and Namibia at 30°S. These oscillations are also manifest in the SL2013sv tomographic model and the short-wavelength pattern of highs and lows remains consistent along the entire length of the transect. The amplitude match is excellent along the northern end of this transect, but it progressively deteriorates toward the southern tip of Africa where a longer wavelength, ~800 m underprediction becomes evident (Figure 11e). This trend may be related to large-scale upwelling within the lower mantle beneath Africa and is consistent with the ~650 m of air-loaded dynamic support inferred from joint inverse modeling of geochemical and geophysical observations across the southern African region (Colli et al., 2016; Gurnis et al., 2000; Jones et al., 2017; Ritsema et al., 1999).

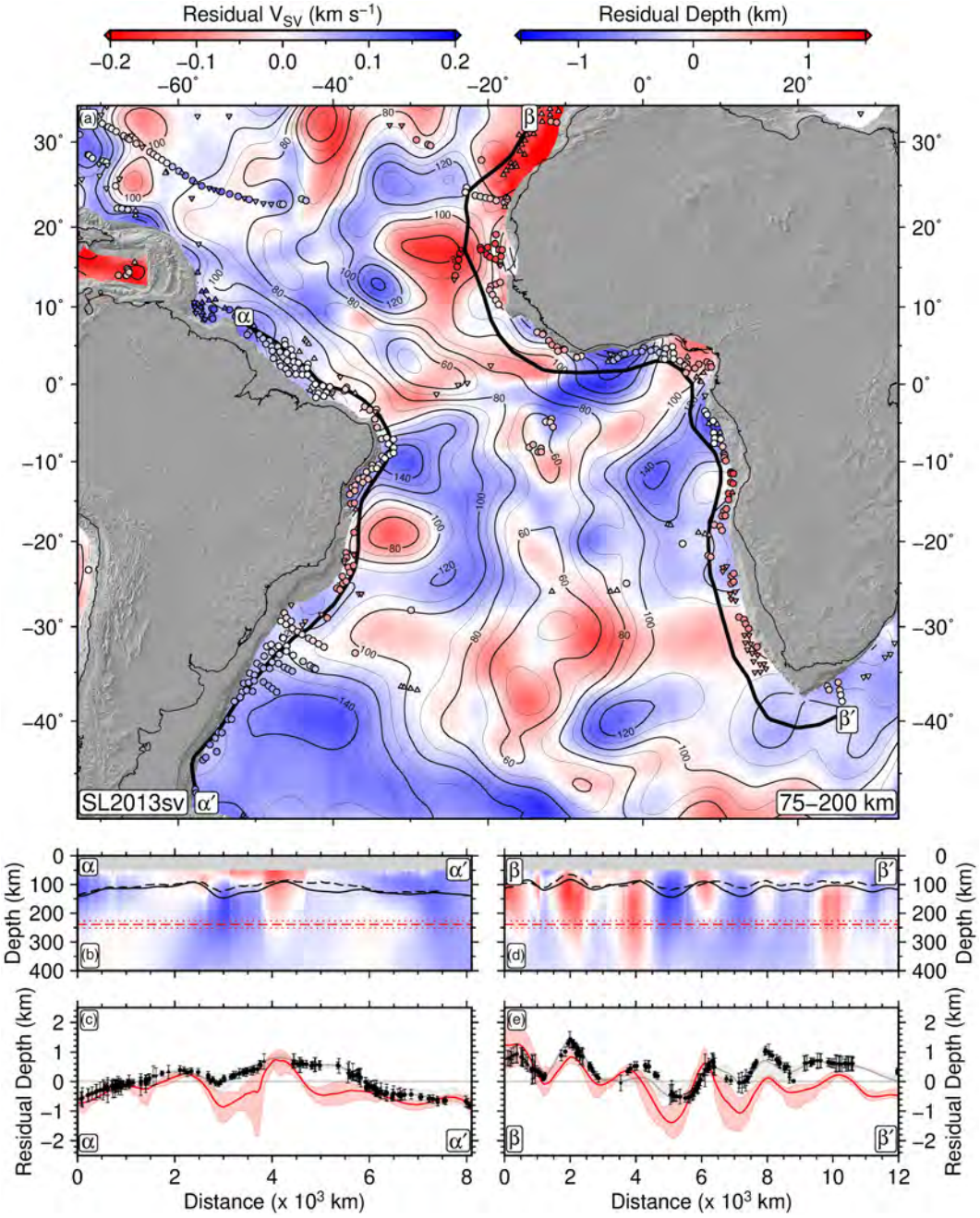

Figure 11. Comparing observed and predicted residual depth along margins of South Atlantic Ocean. (a) Residual shear wave velocity anomalies calculated from SL2013sv model and vertically averaged between depths of 75 km and 200 km. Numbered black lines = contours of depth to 1200°C isothermal surface demarcating lithosphere-asthenosphere boundary; colored circles/triangles = spot measurements of residual depth from Figure 1a; thick black lines labeled α-α' and β-β' = transects shown in panels (b) and (c), respectively. (b) North-to-south transect along South American margin showing residual shear wave velocity anomalies as a function of depth. Solid black line = lithosphere-asthenosphere boundary from contours in panel (a); solid/dashed red lines = assumed ~240±25 km compensation depth; dashed black line = lithosphere-asthenosphere boundary required to exactly match observed residual depth measurements (see Figure 13b). (c) Observed and predicted water-loaded residual depth along South American margin. Solid circles/triangles with error bars = spot measurements and their uncertainties; gray line with band = spherical harmonic fit to spot measurements ($l_{max} = 30$); red line with band = predictions from Figure 10a. Uncertainty bands calculated from maximum variation of residual depth within 500 km-wide swath perpendicular to transect. (d) Same as panel (b) for transect along West African margin. (e) Same as panel (c) for African margin.

We note that a component of the misfit within the central segment of the transect is caused by minor (i.e., <400 km) phase shifts of the quasi-sinusoidal pattern that are visible between ranges of 3,000 km and 7,000 km on Figure 11e. These horizontal offsets may be an artifact if there is systematic displacement in

the location of velocity anomalies resulting from the low density of crossing ray paths along this part of the West African margin (Rawlinson et al., 2014; Schaeffer & Lebedev, 2013). In any case, such offsets are close to the horizontal resolving power of surface wave tomographic models, which is typically several hundred kilometers (Priestley & McKenzie, 2013).

6.2.2. Australian Margins

The observational database of residual depth measurements around Australia is dense (Czarnota et al., 2013). There is particularly good coverage on the Northwest Shelf, along the western Australian margin, and across the Great Australian Bight, which together form a continuous transect (Figure 12a). The age of oceanic lithosphere that abuts these margins is more diverse compared with the South Atlantic Ocean. Large negative residual depth anomalies characterize the Great Australian Bight, where oceanic lithosphere is as young as ~60 Ma. Along the western margin up to the Northwest Shelf, residual depths are generally ~1 km shallower with positive excursions of several hundred meters in places. The overall offset between these two regions exists regardless of the reference lithospheric cooling model (Hoggard et al., 2016). Although data coverage is similar to that of the South Atlantic Ocean, the typical wavelength of residual depth variation is longer (~5,000 km). This difference enables us to appraise the predictive power of the calibrated SL2013sv tomographic model in a region where deeper mantle structure may be more influential.

There is a fairly good spatial correlation between residual V_{SV} anomalies and spot measurements of residual depth around the Australian margins (Figure 12a; Czarnota et al., 2013). In the south, a combination of negative dynamic topography and inferred cold temperatures in the Australian-Antarctic discordance are corroborated by the existence of an anomalously depressed mid-ocean ridge, which sits at a depth of 4 km, and by elevated Na_8 values (Gale et al., 2014). If we exclude density anomalies within the lithosphere, there is particularly strong agreement with observed residual depth, such that ~90% of spot measurements that are corrected for both sedimentary and crustal thickness variations are matched within the bounds of uncertainty. Consequently, the lithospheric contributions appear to be responsible for significant misfit adjacent to the western Australian margin, where fast shear wave velocities within the upper 100 km are potentially being smeared out from the Yilgarn and Pilbara cratonic lithosphere (Figure 12c). This mismatch may therefore be related to tomographic modeling artifacts, or reflect increased uncertainty in the anelastic calibration at colder temperatures. Nevertheless, the quality of the fit between observed residual depths and our predictions based on calibrated tomographic models is improved relative to inferences obtained by scaling long-wavelength free-air gravity anomalies using a constant value of admittance (cf. Czarnota et al., 2013).

7. Lithospheric Thickness Changes

Our global analysis of oceanic upper mantle density structure shows promising correlations with shorter wavelength (i.e., <5,000 km) components of observed residual depth. Given that seismic tomography models have finite resolution, we now wish to explore the extent to which lithospheric thickness would need to be modified to fully reconcile observed residual depth with predictions using upper mantle density structure alone. As before, we have used the depth of the 1200°C isothermal surface as a proxy for lithospheric thickness (Figure 13a). This map shows that although lithospheric thickening with increasing age is the dominant trend, many regional deviations are evident including anomalously thin areas that are often associated with magmatic hot spots (e.g., Iceland, Cape Verde, Cameroon volcanic line). Although thickness deviations are typically no greater than ±30 km, they can generate significant residual depth anomalies since steep temperature gradients exist within the conductive lid of the thermal boundary layer.

Here, we calculate the change in observed lithospheric thickness that is required to perfectly match spot measurements of residual depth throughout the oceanic realm. In locations where predicted residual depth is too deep, the effect of lithospheric thinning is approximated by replacing dense lithospheric material with asthenospheric mantle at a potential temperature that is equal to the local average value between the originally determined lithosphere-asthenosphere boundary and the base of the asthenospheric channel at ~240 km. Lithospheric density structure is then recalculated by assuming a constant geothermal gradient between 0°C at the surface and 1200°C at the revised lithosphere-asthenosphere boundary. This replacement continues until the difference in lithostatic pressure at the base of the asthenosphere is equal to that required to fit the observations. In regions where predicted residual depth is too shallow and lithospheric

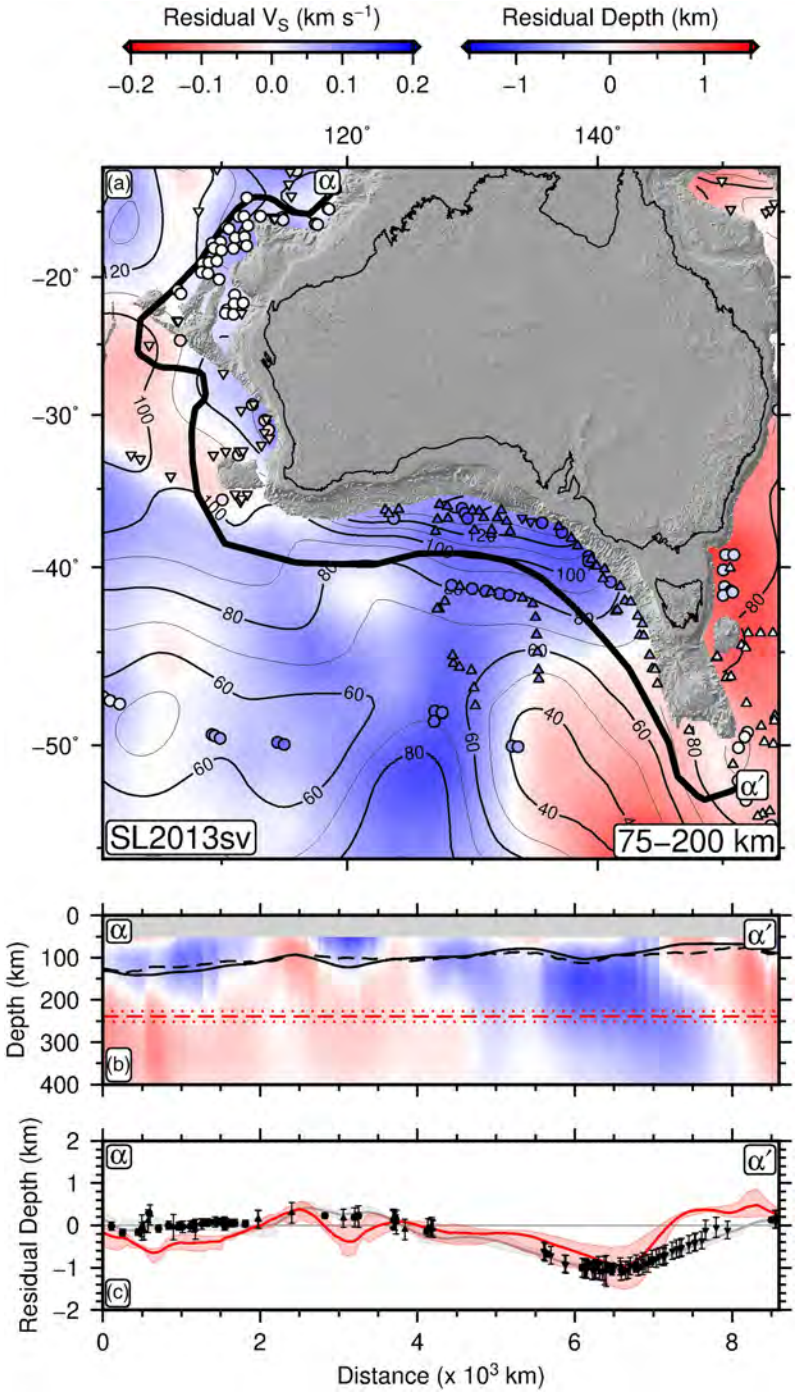

Figure 12. Comparing observed and predicted residual depth along margins of Australia. (a) Residual shear wave velocity anomalies calculated from SL2013sv model and vertically averaged between depths of 75 km and 200 km. Numbered black lines = contours of depth to 1200°C isothermal surface demarcating lithosphere-asthenosphere boundary; colored circles/triangles = spot measurements of residual depth from Figure 1a; thick black lines labeled α-α' and β-β' = transects shown in panels (b) and (c), respectively. (b) Northwest-to-southeast transect along margin showing residual shear wave velocity anomalies as a function of depth. Solid black line = lithosphere-asthenosphere boundary from contours in panel (a); solid/dashed red lines = assumed ~240±25 km compensation depth; dashed black line = lithosphere-asthenosphere boundary required to exactly match observed residual depth measurements (see Figure 13b). (c) Observed and predicted water-loaded residual depth. Solid circles/triangles with error bars = spot measurements and their uncertainties; gray line with band = spherical harmonic fit to spot measurements ($l_{max} = 30$); red line with band = predictions from Figure 10a. Uncertainty bands calculated from maximum variation of residual depth within 500 km-wide swath perpendicular to transect.

thickening is required, a similar procedure is followed except that asthenospheric material of a given potential temperature is replaced by lithospheric mantle whose density is calculated by assuming a constant geothermal gradient.

The resultant global map of modified lithospheric thickness provides an exact match between observed and calculated residual depths by only considering upper mantle density anomalies (Figure 13b). This map is similar in many respects to our original lithospheric thickness map, requiring typical modifications of no more than ±30 km (Figure 13c). This finding suggests that short-wavelength discrepancies between observed and predicted residual depth could potentially be reconciled by invoking minor modifications of lithospheric thickness that are at or below the vertical resolution of tomographic models. Nonetheless, there is a significant offset between the original and modified lithospheric thickness at long wavelengths, with thinner lithosphere required around most of Southern Africa and the West Pacific Ocean, and thicker lithosphere needed across much of southeast Asia and the Americas (Figure 13c). It is unlikely that tomographic models would systematically overestimate or underestimate shear wave velocity anomalies on wavelengths of $\sim 10^4$ km. Instead, we suggest that these longer wavelength discrepancies, which appear to correlate with non-hydrostatic geoid height undulations at $l = 2$, reflect the contribution to observed residual depth from convective flow in the lower mantle (Steinberger et al., 2017).

8. Asthenospheric Viscosity

The anelastic calibration includes a constraint whereby the average diffusion creep viscosity over a depth range of 225–400 km equals the bulk upper mantle viscosity of 3×10^{20} Pa s obtained from glacial isostatic adjustment analysis (Lau et al., 2016). Apart from this bulk constraint, viscosity is free to vary spatially and between depth slices, yielding local estimates for each tomographic model. Although there are currently no independent high-resolution measurements of viscosity beneath oceanic lithosphere, indirect constraints have been inferred from seismic observations. These studies rely on the fact that when mantle flow is accommodated by dislocation as opposed to diffusion creep, a preferential alignment of olivine crystal *c*-axes is expected, such that the seismically fast orientation is parallel to the prevailing mantle flow direction (Zhang & Karato, 1995). The strength of this rotational alignment is predicted to have a maximum value where shear strain gradients are greatest (Hansen et al., 2016). This lattice-preferred orientation (LPO) causes horizontally polarized shear waves to travel faster than vertically polarized shear waves through the asthenosphere (i.e., $V_{SH} > V_{SV}$; Dziewonski & Anderson, 1981). Seismic evidence for significant azimuthal anisotropy at asthenospheric depths has therefore been used to infer that deformation and flow within this region predominantly occurs by dislocation rather than by diffusion creep (Karato & Wu, 1993).

In order to investigate the seismic character and fabric of what is regarded as "normal" oceanic upper mantle, the NoMelt seismic experiment was carried out on Late Cretaceous seafloor within the middle of the Pacific plate at a location that is remote from hot spot volcanism, approximately 1,200 km southeast of Hawaii (Lin et al., 2016). The study reported strong variations in both the amplitude and the orientation of azimuthal anisotropy within the upper mantle, including a marked peak in the strength of anisotropy at a depth of ~225 km (Figure 14a). Significantly, the orientation of the fast direction at depths that are shallower than 100 km and deeper than 250 km is aligned with the fossil spreading direction, but deviates by ~20° for intermediate depths (Figure 14b). This observation is interpreted as evidence for partially decoupled motion between the asthenosphere and lithosphere, which is favored by the existence of a low-viscosity asthenospheric channel.

We can exploit this setting to test whether or not inferences about mantle flow derived from these measurements of seismic anisotropy are consistent with independently determined rheological constraints provided by our anelastic parameterization. The V_S-derived temperature profile for this region suggests that lithosphere is ~80 km thick, assuming that the lithosphere-asthenosphere boundary coincides with the depth to the 1200°C isothermal surface (Figure 14c). Although the lithosphere-asthenosphere system is not necessarily in thermal steady state, we can calculate the approximate base of the thermal boundary layer by fitting a geothermal profile using the method described by Mather et al. (2011). For this calculation, we adopt the temperature- and pressure-dependent thermal conductivity parameterization for oceanic crust and mantle of Korenaga and Korenaga (2016), we use a potential temperature of 1333°C, and we assume a kinematic viscosity of 9×10^{16} m^2 s^{-1}. We obtain an inferred base of the thermal boundary layer at ~120 km depth.

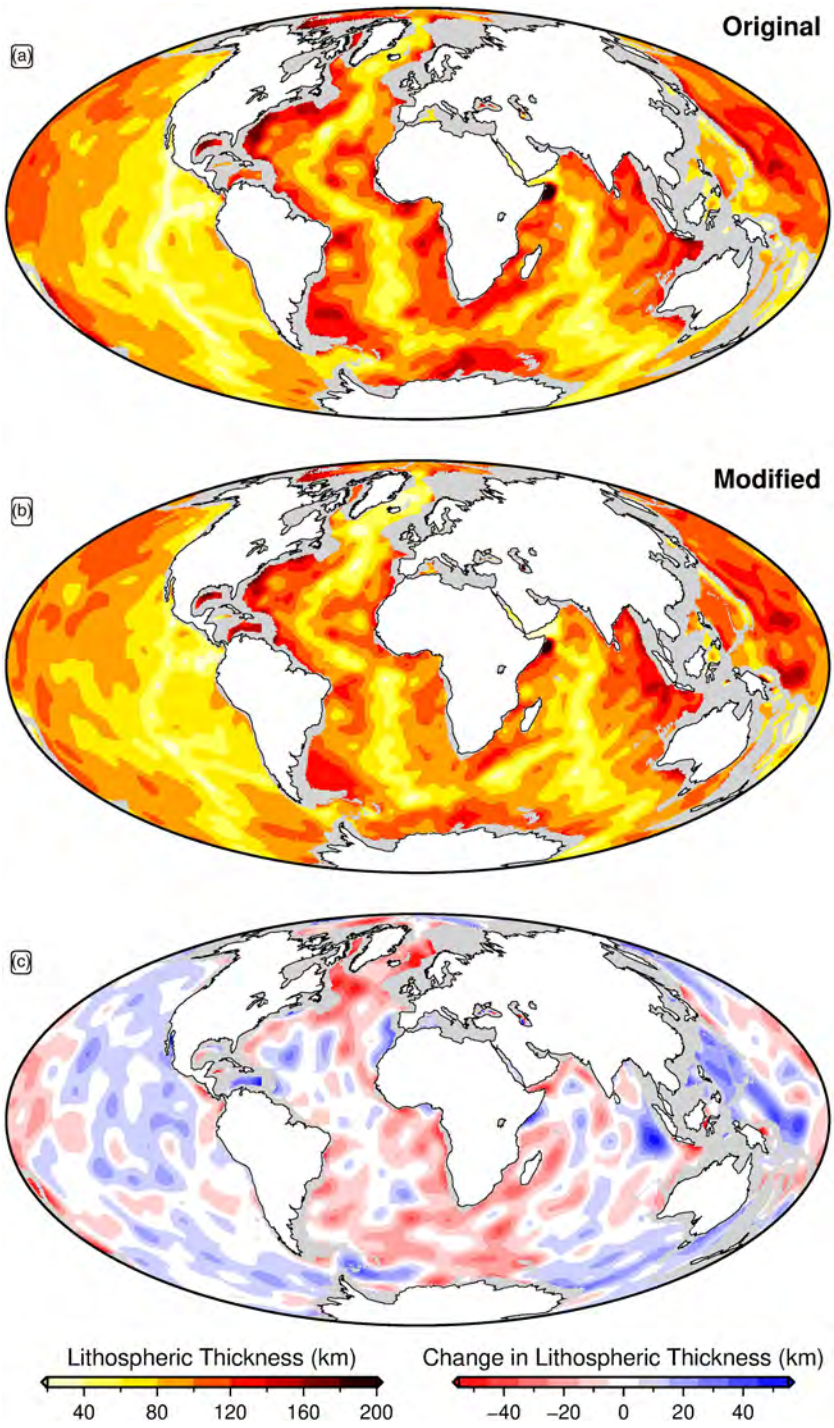

Figure 13. Lithospheric thickness calculations. (a) Lithospheric thickness of oceanic plates (i.e., depth to 1200°C isothermal surface) determined from calibrated SL2013sv model. (b) Tuned lithospheric thickness obtained by minimizing misfit between observed and predicted residual depths. (c) Required modification of lithospheric thickness obtained by subtracting panel (b) from (a).

Anelastic calibration of the SL2013sv model provides a direct estimate of the steady-state diffusion creep viscosity profile beneath the NoMelt experiment. However, the seismic evidence is indicative of dislocation creep, whereby viscosity is a function of the strain rate in addition to temperature (Hirth & Kohlstedt, 2003; Karato & Wu, 1993). Although there is no independent observational constraint on the strain rate profile beneath the NoMelt location, this region is thought to be representative of typical upper mantle

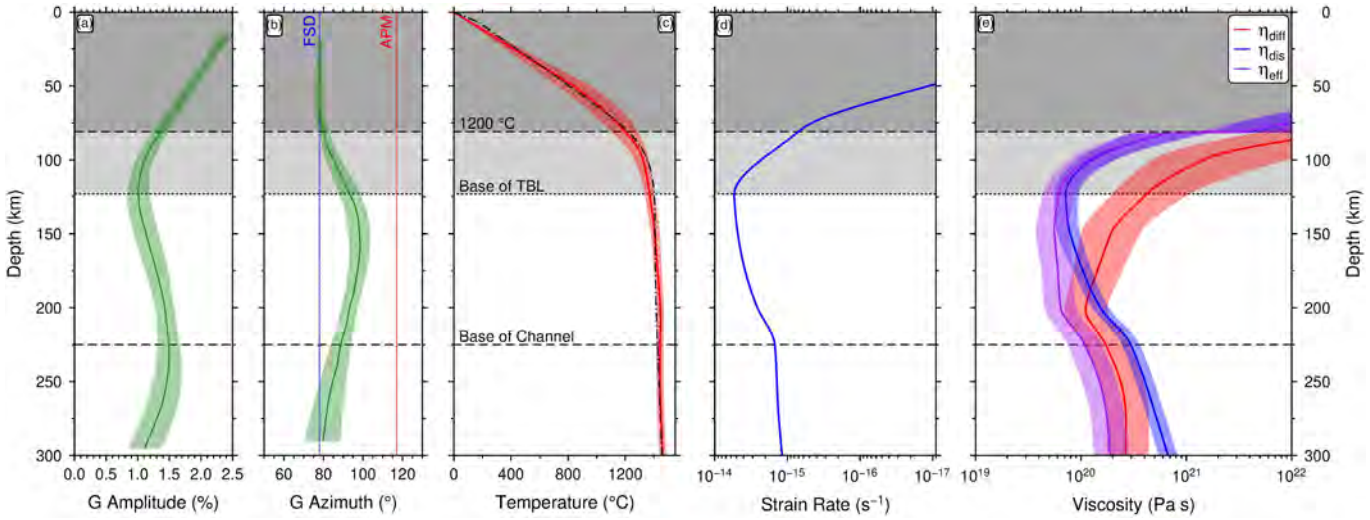

Figure 14. Seismologic constraints on viscosity and mantle flow from Pacific Ocean. (a) Mean and standard deviation of seismic anisotropy, *G*, amplitude as a function of depth from NoMelt experiment, redrawn from Lin et al. (2016). Other lines and shading are labeled in panel (c). (b) Mean and standard deviation of *G* azimuth as a function of depth. Blue line labeled FSD = fossil spreading direction; red line labeled APM = absolute plate motion direction. (c) Mean temperature profile as a function of depth for radius of 500 km centered on location of NoMelt seismic array (approximately 9.5°N, 145.5°W). Red line with band = temperature profile and its uncertainty calculated from calibrated SL2013sv model; dotted-dashed black line = best-fit steady-state geothermal profile. Labeled horizontal dashed lines = base of mechanical boundary layer defined by depth to 1200°C isothermal surface, base of thermal boundary layer (TBL) defined by steady-state geothermal profile, and base of asthenospheric channel. (d) Average oceanic strain rate plotted as a function of depth calculated from model of mantle flow that assumes upper mantle water concentration of 100 H/10^6 Si (Osei Tutu et al., 2018). (e) Three inferred mean viscosity profiles. Red line with band = diffusion creep viscosity, η_{diff}, and its uncertainty calculated from calibrated SL2013sv model; blue line with band = dislocation creep viscosity, η_{dis}, and its uncertainty calculated using combination of temperature profile in panel (c) and strain rate profile in panel (d), using activation parameters given by Osei Tutu et al. (2018); purple line with band = effective viscosity, η_{eff}, and its uncertainty.

conditions in the oceanic realm. We therefore extract an average oceanic strain rate profile obtained by Osei Tutu et al. (2018) from global mantle flow models that assume a water concentration of 100 H/10^6 Si in the top 300 km of the mantle. In their models, mantle flow beneath 300 km is calculated using a spectral method, assuming the radial viscosity profile of (Steinberger & Calderwood, 2006). This flow prediction is then mechanically coupled at 300 km depth to a finite-element model that uses an age-dependent three-dimensional thermal structure and a composite diffusion-dislocation creep rheology. By adopting the oceanic strain rate profile produced by this model together with their dislocation creep activation parameters, we use the V_S-derived temperature profile to predict a dislocation creep viscosity profile. Dislocation and diffusion creep viscosities can then be combined to generate a profile of effective viscosity, η_{eff}, using

$$\eta_{eff} = \frac{\eta_{diff}\eta_{dis}}{\eta_{diff} + \eta_{dis}} \tag{26}$$

where η_{diff} is the diffusion creep viscosity and η_{dis} is the dislocation creep viscosity (Figure 14e).

Within the lithosphere, viscosity values are uniformly high (i.e., 10^{22} Pa s), but rapidly decrease with depth toward the thermal boundary layer. Here, dislocation creep viscosities are 1 order of magnitude lower than those for diffusion creep, so this mechanism controls the calculated value of η_{eff}. The thermal boundary layer is underlain by a ~100 km-thick low-viscosity asthenospheric channel where $\eta_{eff} \sim 5 \times 10^{19}$ Pa s. At its base, over the 200–250 km depth range, diffusion creep viscosity becomes lower than that for dislocation creep and starts to dominate the calculated value of η_{eff}. This transition coincides with a factor of 4 increase in effective viscosity, suggesting that the low-viscosity channel has a relatively sharp base. These features remain consistent, irrespective of whether a constant grain size model is used or whether radial variations from the model of Dannberg et al. (2017) are adopted. In both cases, the predicted viscosity profile is consistent with glacial isostatic adjustment and mantle convection studies (Mitrovica & Forte, 2004; Steinberger & Calderwood, 2006).

Our inferences about viscosity are also compatible with the observations of seismic anisotropy. The peak in the amplitude of azimuthal anisotropy is aligned with the base of the low-viscosity channel (Figure 14a). Furthermore, maximum azimuthal deviation away from the fossil spreading direction coincides with a viscosity minimum at ~150 km depth (Figure 14b). These observations imply that channelized Poiseuille or plug flow is occurring within the asthenosphere. In this configuration, shear strain gradients responsible for aligning minerals peak at the viscosity contrasts that define the channel boundaries, while flow velocities are expected to be fastest in the center, maximizing azimuthal rotation away from the prevailing directions outside the channel (Semple & Lenardic, 2018). Given the remoteness of the NoMelt location from hot spot magmatism, the presence of a low-viscosity channel suggests that these flow regimes are not necessarily confined to the vicinity of upwelling plumes (Morgan & Smith, 1992; Natarov & Conrad, 2012; Stotz et al., 2018).

Indeed, we find evidence for a low-viscosity asthenosphere throughout the oceanic realm. It is particularly well developed beneath young lithosphere in the vicinity of magmatic hot spots (e.g., Iceland and Galapagos) where diffusion creep viscosity can increase by up to a factor of 50 from the channel center into the underlying mantle. Beneath the oldest oceanic lithosphere remote from magmatic hot spots, this viscosity increase drops by a factor of 2 to 3. These observations suggest that channelized flow may be pervasive, thus helping to justify the thermal isostatic approximation used in Equation 25 to predict residual depth. We infer that lithospheric and asthenospheric density contributions are effectively decoupled from deeper mantle flow. This inference is compatible with surface topography kernels, which approach unity within the shallowest mantle for all spherical harmonic degrees, with kernels of higher degree rapidly decaying to 0 beneath the base of the asthenospheric channel.

We have also shown that a relatively low-viscosity oceanic asthenosphere is consistent with attenuation and shear wave velocity profiles, but throughout this analysis, have implicitly assumed that temperature and pressure are the principal controls on seismic structure. While variations in these properties are generally believed to dominate upper mantle rheology, variations in grain size, composition, and water content also influence diffusion creep viscosities (Behn et al., 2009; Dannberg et al., 2017; Karato & Jung, 1998; Ma & Dalton, 2019). The impact of these additional factors on both anharmonic velocities and anelasticity is a topic for future research.

9. Implications for Dynamic Topography

We have shown that adoption of a simple isostatic approximation and omission of deeper mantle flow yields reasonable fits between predicted and observed oceanic residual depths. We now wish to incorporate our tomographically inferred upper mantle density structure into more physically realistic models of whole-mantle flow to generate new global predictions of dynamic topography. Our goals are to explore the spectral implications of these revised models and to investigate the extent to which observed residual depth is supported by buoyancy anomalies within the convecting mantle versus those associated with the lithosphere.

9.1. Instantaneous Flow Calculations

We exploit the instantaneous flow methodology outlined in section 2 that was originally implemented by Hager and O'Connell (1979) and subsequently updated to include the effects of compressibility and self-gravitation by Corrieu et al. (1995). As a result of this update, in addition to their dependence on the chosen radial viscosity profile, the sensitivity kernels have a weak dependence upon radial variations of the degree zero component (i.e., layer average) of the density structure. These calculations also require several other parameter choices. We impose free-slip boundary conditions both at the surface and at the core-mantle boundary (i.e., vertical velocities and shear stresses vanish at these interfaces). The surface is assumed to be water-loaded, whereby radial normal stresses are balanced using a seawater density of 1,030 kg m^{-3}. To calculate deflections of the core-mantle boundary, we set the density of the outer core to 9,900 kg m^{-3}. Here, we present results using the radial viscosity profile presented by Steinberger et al. (2010), which is consistent with geoid, glacial isostatic adjustment and heat flow constraints. Alternative models using different viscosity profiles are presented in the supporting information (Forte et al., 2010; Mitrovica & Forte, 2004). It is important to emphasize that most viscosity profiles incorporate a high viscosity lithospheric lid underlain by a low-viscosity asthenospheric layer, which yields surface response kernels

that approach unity (i.e., isostatic equilibrium) for the lithosphere and shallow asthenosphere. Therefore, we can calculate surface deflections caused both by buoyancy within the convecting mantle and by buoyancy associated with lithospheric density anomalies that depart from the plate cooling relationship, in accordance with our definition of dynamic topography.

To determine density structure, we combine our upper mantle model inferred by anelastic parameterization of SL2013sv with a deeper mantle model. It is generally agreed that the upper ~400 km of the mantle is dominated by olivine. However, there is ongoing debate about how shear wave velocity anomalies should be converted into density within the middle and lower mantle. This controversy is exacerbated by poorer seismic resolution, by the paucity of mineral physics constraints at relevant pressures and temperatures, by significant and poorly understood changes in physical properties across phase transitions, and by the potential presence of compositional heterogeneities within the lower mantle (Connolly & Khan, 2016; Garnero et al., 2016; Koelemeijer et al., 2018; Lau et al., 2017; Schuberth & Bunge, 2009; Stixrude & Lithgow-Bertelloni, 2012). Despite these scientific challenges, estimates of mantle density structure have been obtained by simultaneously inverting seismologic data and geodynamic observables, such as long-wavelength gravity anomalies and excess ellipticity of the core-mantle boundary (e.g., Simmons et al., 2009). Here, we use density variations from the TX2008 joint inversion of Simmons et al. (2009) around a reference radial profile derived from PREM (i.e., Preliminary Reference Earth Model; Dziewonski & Anderson, 1981). We note that the sensitivity of surface topography kernels for degrees that are greater than $l = 8$ is minimal for the lower mantle, and so resolution limitations are less problematic than for the upper mantle (Figure 2c).

To ensure a smooth transition between the two models, our hybrid mantle model uses their weighted average between 300 km and 400 km, beyond which the sensitivity of surface waves tends to 0. The weighting coefficients of the respective tomographic models, w_s and w_t, vary linearly between 1 and 0 over this depth range and are combined according to $w_s = 1 - w_t$. Based on analyses of heat flow measurements, xenolith geochemistry, seismic velocity, gravity, and topography, it has been proposed that compositional and thermal density contributions approximately balance each other (in the isopycnal sense) beneath continental lithosphere (Jordan, 1978; Shapiro et al., 1999). Therefore, we set density of the continental lithosphere, delineated by the $T = 1200$°C isothermal surface, equal to the average density of all external material at the relevant depth. The resultant whole-mantle density field is then interpolated at ~11 km depth increments from the surface to the core-mantle boundary. Each of the 257 equally spaced layers is expanded in spherical harmonic functions up to degree and order 50.

9.2. Quantifying Buoyancy Sources

In the upper mantle, our density deviations represent a combination of temperature anomalies within the convecting mantle, variations in lithospheric thickness, and temperature anomalies within the lithosphere. The relative importance of these contributions to the total amplitude of predicted dynamic topography remains controversial (Davies et al., 2019; Hoggard et al., 2020a). Isolating these different contributions is not trivial due to ambiguity in the appropriate reference conditions and the limited vertical resolution of tomographic models, which leads to a degree of covariation between these sources. Nevertheless, to tackle this question, we perform calculations using our whole-mantle density model, which includes all buoyancy contributions, and a modified version. This modified model is constructed by removing the effect of deviations in lithospheric thickness away from the assumed average oceanic behavior and density anomalies that reside within the lithosphere.

We begin by determining a suite of reference temperature profiles as a function of lithospheric thickness using theoretical cooling models. Since there are locations with lithosphere of greater thickness than the maximum obtained by the plate cooling model, all reference temperature profiles are derived from an equivalent half-space cooling parameterization ($T_p = 1333$°C; Richards et al., 2018). For seafloor of a given age, the expected lithospheric thickness is taken from the plate cooling model and used to select an appropriate reference temperature profile. A second profile is then selected using the local lithospheric thickness inferred from the tomographic model. At each oceanic location, the difference as a function of depth between these two profiles is used to calculate density anomalies associated with local lithospheric thickness deviations alone. These departures are subsequently subtracted from the unmodified model. Finally, we remove additional density anomalies located within the lithosphere by rendering them neutrally buoyant.

This correction is implemented by setting all densities shallower than the $T = 1200°C$ isothermal surface to a constant value equivalent to the mean density of material outside the lithosphere at this depth.

By adjusting the integration limits of Equation 1, we first calculate dynamic topography generated by the top 400 km of the mantle alone (Figures 15a and 15c). For the modified density structure where lithospheric contributions are ignored, a correlation of $r = 0.40$ is obtained between observed and predicted residual depth (Figure 15b). The slope of the best-fit linear relationship is m~0.6. The gradient of the power spectrum for $l > 8$ matches that of the observations, but the amplitudes are ~30% too low (Figure 15g). However, when the lithospheric contributions are also included, the correlation improves to $r = 0.54$, the slope increases to m~0.9, and the power spectrum agrees with that of the observations for $l > 8$ (Figures 15d and 15g). These values illustrate the importance of incorporating shallow mantle structure to accurately reproduce short-wavelength dynamic topography, and indicate that buoyancy contributions from the convecting mantle provide approximately twice as much topography as those from the lithosphere. Oceanic lithospheric contributions are dominated by deviations in thickness away from the age-dependent average, with internal anomalies contributing <10% of the total amplitude.

The most striking outcome of these flow calculations, despite only accounting for density contributions from the upper 15% of the mantle, is that our revised upper mantle predictions yield an improved fit to observed residual depth compared to previously published models based upon whole-mantle flow (Conrad & Husson, 2009; Davies et al., 2019; Flament et al., 2013; Ricard et al., 1993; Spasojevic & Gurnis, 2012; Steinberger, 2007). Nevertheless, the power spectra of these upper mantle predictions clearly have insufficient spectral power for $l \leq 8$ (Figure 15g). At these longer wavelengths, surface topography kernels indicate that buoyancy anomalies within the lower mantle will also contribute to dynamic topography (Figure 2c). If we instead account for all buoyancy contributions throughout the whole mantle, predicted dynamic topography has amplitudes of ± 2 km and point-wise residual depth correlations of $r = 0.57$ (Figures 15e and 15f). Although, the slightly larger value of $m = 1.15$ suggests that dynamic topography is marginally overpredicted, the spectral properties at $l \leq 8$ are now significantly more compatible with observations without degrading the fit at shorter wavelengths (Figure 15g). In addition, this model yields a satisfactory fit to non-hydrostatic geoid anomalies ($r = 0.91$; supporting information Figure S4). These results are moderately sensitive to the choice of viscosity profile and demonstrate that it is generally possible to simultaneously reconcile observed geoid height anomalies with appropriately modest amplitudes for long-wavelength dynamic topography (supporting information Figures S5–S6; cf. Coltice et al., 2017).

Irrespective of whether upper or whole-mantle anomalies are considered, our predicted dynamic topography is symmetrically distributed about 0, which is in better agreement with observational constraints and with fluid dynamical expectations for a vigorously convecting mantle (Figure 15h; Hoggard et al., 2017; Jarvis & Peltier, 1986). We infer that both lithospheric deviations and asthenospheric temperature anomalies are required to generate observed short-wavelength residual depth. When whole-mantle flow is considered, approximately one quarter of the surface deflections in oceanic regions can be accounted for by lithospheric contributions. This preliminary conclusion may differ within the continents, where larger variations in the thickness and density structure of lithosphere are likely to have a stronger influence on residual topography. We believe that the improved fit we obtain at short wavelengths compared with results presented by Steinberger et al. (2017) and Davies et al. (2019) is principally a consequence of using an appropriately calibrated anelastic parameterization for converting shear wave velocity into density in the upper mantle. This parameterization generates less extreme density variations, which helps to produce amplitudes of dynamic topography that are more consistent with residual depth measurements.

10. Conclusions

In order to accurately convert shear wave velocities into temperature and density with a view to constraining upper mantle structure, it is important to account for the effects of anelasticity at seismic frequencies. Here, we refine an existing inverse approach that individually calibrates a laboratory-derived anelastic parameterization for different tomographic models. The method exploits the temperature structure of a cooling oceanic plate in combination with deeper mantle constraints that include the isentropic geothermal profile, seismic attenuation measurements, and inferences of bulk upper mantle viscosity. It yields self-consistent estimates of temperature, density, and diffusion creep viscosity.

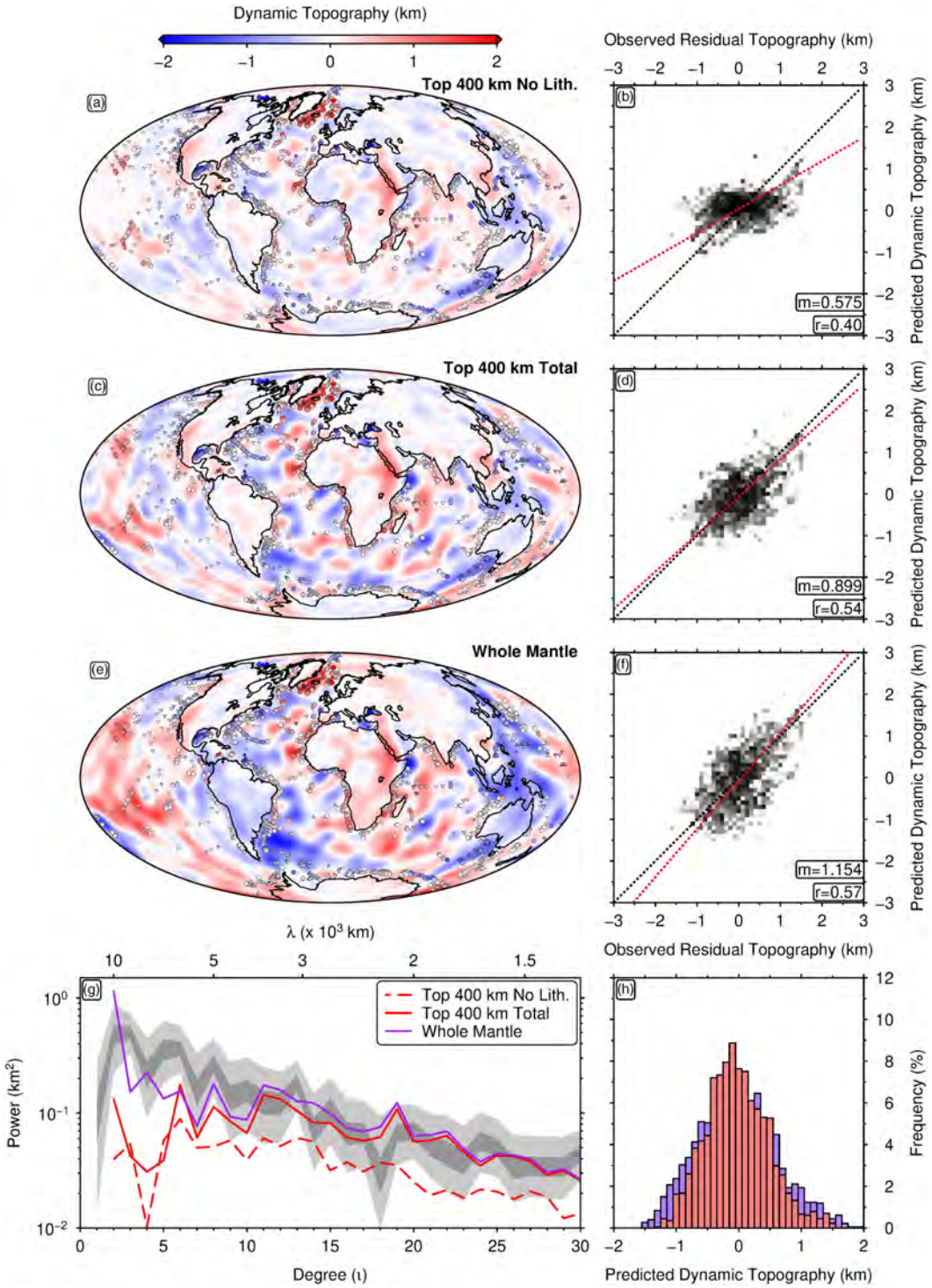

Figure 15. Instantaneous flow calculations. (a) Predicted $l = 2$–30 dynamic topography for upper 400 km of mantle density model, excluding lithospheric contributions. Calculations use radial viscosity profile of Steinberger et al. (2010). Deflections are air-loaded onshore and water-loaded offshore; circles/triangles = spot measurements of residual depth from Figure 1a. (b) Observed residual depth plotted against predicted dynamic topography. Black line = 1:1 relationship; r = Pearson's correlation coefficient; red line = best-fit linear relationship with slope m. (c, d) Same for mantle density anomalies above 400 km with lithospheric contributions included. (e, f) Same for whole-mantle density anomalies with lithospheric contributions included. (g) Comparison of observed and predicted power spectra. Dark/light gray envelope = 99%/50% confidence intervals about mean power spectrum of oceanic residual depth measurements constructed using Automatic Relevance Determination algorithm (Davies et al., 2019). (h) Histograms of predicted dynamic topography at loci of spot measurements of residual depth. Red bars = values from panel (c) calculated using upper mantle density anomalies alone; purple bars = values from panel (e) calculated using density anomalies throughout the whole mantle.

Our revised mantle temperature estimates are corroborated by independent observations that include oceanic crustal thickness measurements, Na_8 values from mid-ocean ridge basalts, and axial ridge depths. Locally determined diffusion creep viscosity and inferred values for dislocation creep viscosity are consistent with independent observations of seismic anisotropy from the Pacific Ocean. In agreement with the work of others, we infer the presence of Poiseuille or plug flow within an asthenospheric channel that is ~150 km thick and has an effective viscosity at least four times lower than the underlying upper mantle.

Finally, our improved models of mantle buoyancy structure can be used to assess the extent to which dynamic topography arising from mantle flow can account for observational estimates of oceanic residual depth. We construct a hybrid density model by combining a previously published whole-mantle model obtained by joint inverse modeling of seismic and geodynamic observables with our revised upper mantle structure. For wavelengths <5,000 km, we find that anomalies within the convecting mantle can support ~75% of observed amplitudes. The remainder is supported by local deviations in lithospheric structure that depart from the idealized plate cooling relationship. Buoyancy structure of the lower mantle is mostly responsible for dynamic topography at wavelengths >5,000 km. Whole-mantle predictions of dynamic topography outperform previous predictive models, yielding a correlation coefficient of $r = 0.57$ when observed and calculated spot residual depths are compared. Significantly, we also obtain satisfactory fits to the non-hydrostatic geoid. Our results demonstrate that it is essential to include accurate models of upper mantle density structure when reconstructing both present-day dynamic topography and its spatiotemporal evolution.

Data Availability Statement

The data upon which this article is based are available within Gale et al. (2014) and Hoggard et al. (2017).

Acknowledgments

This work was partly funded by a BP-Cambridge collaboration. F. R. acknowledges support from the Imperial College Research Fellowship scheme and the Schmidt Science Fellows program, in partnership with the Rhodes Trust.. M. H. acknowledges support from the National Aeronautics and Space Administration (Grant NNX17AE17G) and from the American Chemical Society Petroleum Research Fund (59062-DNI8). C. Dalton and N. Flament provided helpful reviews. We also thank J. C. Afonso, J. Gaherty, S. Goes, B. Holtzman, C. McCarthy, D. McKenzie, J. Mitrovica, P. Nimis, K. Priestley, D. Schutt, S. Stephenson, and Y. Takei for help and discussion. The authors declare no competing financial interests. University of Cambridge Earth Sciences contribution number esc.4821.

References

Adenis, A., Debayle, E., & Ricard, Y. (2017). Attenuation tomography of the upper mantle. *Geophysical Research Letters*, *44*, 7715–7724. https//doi.org/10.1002/2017GL073751

Becker, T. (2002). A comparison of tomographic and geodynamic mantle models. *Geochemistry, Geophysics, Geosystems*, *3*(1), 1003. https//doi.org/10.1029/2001GC000168

Behn, M. D., Hirth, G., & Ii, J. R. E. (2009). Implications of grain size evolution on the seismic structure of the oceanic upper mantle. *Earth and Planetary Science Letters*, *282*(1-4), 178–189. https//doi.org/10.1016/j.epsl.2009.03.014

Bodin, T., Capdeville, Y., Romanowicz, B., & Montagner, J.-P. (2015). Interpreting radial anisotropy in global and regional tomographic models, *The Earth's heterogeneous mantle* (pp. 105–144). Cham: Springer.

Bouhifd, M. A., Andrault, D., Fiquet, G., & Richet, P. (1996). Thermal expansion of forsterite up to the melting point. *Geophysical Research Letters*, *23*(10), 1143–1146. https//doi.org/10.1029/96GL01118

Braun, J. (2010). The many surface expressions of mantle dynamics. *Nature Geoscience*, *3*(12), 825–833. https//doi.org/10.1038/ngeo1020

Burgos, G., Montagner, J. P., Beucler, E., Capdeville, Y., Mocquet, A., & Drilleau, M. (2014). Oceanic lithosphere-asthenosphere boundary from surface wave dispersion data. *Journal of Geophysical Research: Solid Earth*, *119*, 1079–1093. https//doi.org/10.1002/2013JB010528

Cammarano, F., Goes, S., Vacher, P., & Giardini, D. (2003). Inferring upper-mantle temperatures from seismic velocities. *Physics of the Earth and Planetary Interiors*, *138*(3-4), 197–222. https//doi.org/10.1016/S0031-9201(03)00156-0

Cammarano, F., Romanowicz, B., Stixrude, L., Lithgow-Bertelloni, C., & Xu, W. (2009). Inferring the thermochemical structure of the upper mantle from seismic data. *Geophysical Journal International*, *179*(2), 1169–1185. https//doi.org/10.1111/j.1365-246X.2009.04338.x

Cazenave, A., Souriau, A., & Dominh, K. (1989). Global coupling of Earth surface topography with hotspots, geoid and mantle heterogeneities. *Nature*, *340*(6228), 54–57.

Colli, L., Ghelichkhan, S., & Bunge, H.-P. (2016). On the ratio of dynamic topography and gravity anomalies in a dynamic Earth. *Geophysical Research Letters*, *43*, 2510–2516. https//doi.org/10.1002/2016GL067929

Coltice, N., Gérault, M., & Ulvrová, M. (2017). A mantle convection perspective on global tectonics. *Earth-Science Reviews*, *165*, 120–150. https//doi.org/10.1016/j.earscirev.2016.11.006

Connolly, J. A. (2009). The geodynamic equation of state: What and how. *Geochemistry, Geophysics, Geosystems*, *10*, Q10014. https//doi.org/10.1029/2009GC002540

Connolly, J. A. D., & Khan, A. (2016). Uncertainty of mantle geophysical properties computed from phase equilibrium models. *Geophysical Research Letters*, *43*, 5026–5034. https//doi.org/10.1002/2016GL068239

Conrad, C. P., & Husson, L. (2009). Influence of dynamic topography on sea level and its rate of change. *Lithosphere*, *1*, 110–120. https//doi.org/10.1130/L32.1

Corrieu, V., Thoraval, C., & Ricard, Y. (1995). Mantle dynamics and geoid green functions. *Geophysical Journal International*, *120*(2), 516–523. https//doi.org/10.1111/j.1365-246X.1995.tb01835.x

Cottaar, S., Heister, T., Rose, I., & Unterborn, C. (2014). Burnman: A lower mantle mineral physics toolkit. *Geochemistry, Geophysics, Geosystems*, *15*, 1164–1179. https//doi.org/10.1002/2013GC005122

Czarnota, K., Hoggard, M. J., White, N., & Winterbourne, J. (2013). Spatial and temporal patterns of Cenozoic dynamic topography around Australia. *Geochemistry, Geophysics, Geosystems*, *14*, 634–658. https//doi.org/10.1029/2012GC004392

Dalton, C. A., Ekström, G., & Dziewonski, A. M. (2009). Global seismological shear velocity and attenuation: A comparison with experimental observations. *Earth and Planetary Science Letters*, *284*(1-2), 65–75. https//doi.org/10.1016/j.epsl.2009.04.009

Dalton, C. A., Langmuir, C. H., & Gale, A. (2014). Geophysical and geochemical evidence for deep temperature variations beneath mid-ocean ridges. *Science*, *344*(6179), 80–83. https//doi.org/10.1126/science.1249466

Dannberg, J., Eilon, Z., Faul, U., Gassmo'ller, R., Moulik, P., & Myhill, R. (2017). The importance of grain size to mantle dynamics and seismological observations. *Geochemistry, Geophysics, Geosystems*, *18*, 1–28. https//doi.org/10.1002/2017GC006944

Davies, D., Valentine, A., Kramer, S., Rawlinson, N., Hoggard, M., Eakin, C., & Wilson, C. (2019). Earth's multi-scale topographic response to global mantle flow. *Nature Geoscience*, *12*(10), 845–850.

Debayle, E., Dubuffet, F., & Durand, S. (2016). An automatically updated *S*-wave model of the upper mantle and the depth extent of azimuthal anisotropy. *Geophysical Research Letters*, *43*, 674–682. https//doi.org/10.1002/2015GL067329

Dziewonski, A. M., & Anderson, D. L. (1981). Preliminary reference Earth model. *Physics of the Earth and Planetary Interiors*, *25*(4), 297–356. https//doi.org/10.1016/0031-9201(81)90046-7

Eilon, Z. C., & Abers, G. A. (2017). High seismic attenuation at a mid-ocean ridge reveals the distribution of deep melt. *Science Advances*, *3*(5), E1602829.

Ekström, G., Tromp, J., & Larson, E. W. (1997). Measurements and global models of surface wave propagation. *Journal of Geophysical Research*, *102*(B4), 8137–8157.

Faul, U. H., & Jackson, I. (2005). The seismological signature of temperature and grain size variations in the upper mantle. *Earth and Planetary Science Letters*, *234*(1), 119–134. https//doi.org/10.1016/j.epsl.2005.02.008

Faul, U., & Jackson, I. (2015). Transient creep and strain energy dissipation: An experimental perspective. *Annual Review of Earth and Planetary Sciences*, *43*(1), 541–569. https//doi.org/10.1146/annurev-earth-060313-054732

Fei, H., Hegoda, C., Yamazaki, D., Wiedenbeck, M., Yurimoto, H., Shcheka, S., & Katsura, T. (2012). High silicon self-diffusion coefficient in dry forsterite. *Earth and Planetary Science Letters*, *345*, 95–103.

Flament, N., Gurnis, M., & Müller, R. D. (2013). A review of observations and models of dynamic topography. *Lithosphere*, *5*(2), 189–210. https//doi.org/10.1130/L245.1

Forsyth, D. W. (1992). Geophysical constraints on mantle flow and melt generation beneath mid-ocean ridges. *Mantle Flow and Melt Generation at Mid-Ocean Ridges*, *71*, 1–65.

Forte, A. M., Quéré, S., Moucha, R., Simmons, N. A., Grand, S. P., Mitrovica, J. X., & Rowley, D. B. (2010). Joint seismic-geodynamic-mineral physical modelling of African geodynamics: A reconciliation of deep-mantle convection with surface geophysical constraints. *Earth and Planetary Science Letters*, *295*(3-4), 329–341. https//doi.org/10.1016/j.epsl.2010.03.017

French, S., Lekic, V., & Romanowicz, B. (2013). Waveform tomography reveals channeled flow at the base of the oceanic asthenosphere. *Science*, *342*(6155), 227–230. https//doi.org/10.1126/science.1241514

Gale, A., Langmuir, C. H., & Dalton, C. A. (2014). The global systematics of ocean ridge basalts and their origin. *Journal of Petrology*, *55*(6), 1051–1082. https//doi.org/10.1093/petrology/egu017

Gale, A., Laubier, M., Escrig, S., & Langmuir, C. H. (2013). Constraints on melting processes and plume-ridge interaction from comprehensive study of the FAMOUS and North Famous segments, Mid-Atlantic Ridge. *Earth and Planetary Science Letters*, *365*, 209–220. https//doi.org/10.1016/j.epsl.2013.01.022

Garnero, E. J., McNamara, A. K., & Shim, S.-H. (2016). Continent-sized anomalous zones with low seismic velocity at the base of Earth's mantle. *Nature Geoscience*, *9*(7), 481. https//doi.org/10.1038/ngeo2733

Goes, S., Armitage, J., Harmon, N., Smith, H., & Huismans, R. (2012). Low seismic velocities below mid-ocean ridges: Attenuation versus melt retention. *Journal of Geophysical Research*, *117*, B12403. https//doi.org/10.1029/2012JB009637

Grose, C. J., & Afonso, J. C. (2013). Comprehensive plate models for the thermal evolution of oceanic lithosphere. *Geochemistry, Geophysics, Geosystems*, *14*, 3751–3778. https//doi.org/10.1002/ggge.20232

Gurnis, M., Mitrovica, J. X., Ritsema, J., & van Heijst, H.-J. (2000). Constraining mantle density structure using geological evidence of surface uplift rates: The case of the African superplume, *1*(7), 1020. https//doi.org/10.1029/1999GC000035

Gvirtzman, Z., Faccenna, C., & Becker, T. W. (2016). Isostasy, flexure, and dynamic topography. *Tectonophysics*, *683*, 255–271.

Hager, B. H., Clayton, R. W., Richards, M. A., Comer, R. P., & Dziewonski, A. M. (1985). Lower mantle heterogeneity, dynamic topography and the geoid. *Nature*, *313*(6003), 541–545. https//doi.org/10.1038/313541a0

Hager, B. H., & O'Connell, R. J. (1979). Kinematic models of large-scale flow in the Earth's mantle. *Journal of Geophysical Research*, *84*(B3), 1031–1048. https//doi.org/10.1029/JB084iB03p01031

Hansen, L. N., Qi, C., & Warren, J. M. (2016). Olivine anisotropy suggests Gutenberg discontinuity is not the base of the lithosphere. *Proceedings of the National Academy of Sciences of the United States of America*, *113*(38), 10,503–10,506. https//doi.org/10.1073/pnas.1608269113

Herzberg, C., Asimow, P. D., Arndt, N., Niu, Y., Lesher, C. M., Fitton, J. G., et al. (2007). Temperatures in ambient mantle and plumes: Constraints from basalts, picrites, and komatiites. *Geochemistry, Geophysics, Geosystems*, *8*, Q02006. https//doi.org/10.1029/2006GC001390

Hirschmann, M. M. (2000). Mantle solidus: Experimental constraints and the effects of peridotite composition. *Geochemistry, Geophysics, Geosystems*, *1*(10), 1042. https//doi.org/10.1029/2000GC000070

Hirth, G., & Kohlstedt, D. (2003). Rheology of the upper mantle and the mantle wedge: A view from the experimentalists. In J. Eiler (Ed.), *Inside the subduction factory* (pp. 83–105). Washington, D.C: American Geophysical Union (AGU). https//doi.org/10.1029/138GM06

Ho, T., Priestley, K., & Debayle, E. (2016). A global horizontal shear velocity model of the upper mantle from multimode Love wave measurements. *Geophysical Journal International*, *207*(1), 542–561.

Hoggard, M. J., Austermann, J., Randel, C., & Stephenson, S. N. (2020a). Observational estimates of dynamic topography through space and time. In H. Marquardt, M. Ballmer, S. Cottaar, & J. Konter (Eds.), *Mantle convection and surface expressions*, *AGU Geophysical Monograph Series*. Washington, DC: American Geophysical Union.

Hoggard, M. J., Czarnota, K., Richards, F. D., Huston, D. L., Jaques, A. L., & Ghelichkhan, S. (2020b). Global distribution of sediment-hosted metals controlled by craton edge stability. *Nature Geoscience*, *13*, 504–510.

Hoggard, M. J., White, N., & Al-Attar, D. (2016). Global dynamic topography observations reveal limited influence of large-scale mantle flow. *Nature Geoscience*, *9*, 456–463. https//doi.org/10.1038/ngeo2709

Hoggard, M. J., Winterbourne, J., Czarnota, K., & White, N. (2017). Oceanic residual depth measurements, the plate cooling model, and global dynamic topography. *Journal of Geophysical Research: Solid Earth*, *122*, 2328–2372. https//doi.org/10.1002/2016JB013457

Höink, T., Jellinek, A. M., & Lenardic, A. (2011). Viscous coupling at the lithosphere-asthenosphere boundary. *Geochemistry, Geophysics, Geosystems*, *12*, Q0AK02. https//doi.org/10.1029/2011GC003698

Holtzman, B. K. (2016). Questions on the existence, persistence, and mechanical effects of a very small melt fraction in the asthenosphere. *Geochemistry, Geophysics, Geosystems*, *17*, 470–484. https//doi.org/10.1002/2015GC006102

Hu, Y., Bürgmann, R., Banerjee, P., Feng, L., Hill, E. M., Ito, T., et al. (2016). Asthenosphere rheology inferred from observations of the 2012 Indian Ocean earthquake. *Nature*, *538*(7625), 368–372. https//doi.org/10.1038/nature19787
Iaffaldano, G., & Lambeck, K. (2014). Pacific plate-motion change at the time of the Hawaiian-Emperor Bend constrains the viscosity of Earth's asthenosphere. *Geophysical Research Letters*, *41*, 3398–3406. https//doi.org/10.1002/2014GL059763
Isaak, D. G. (1992). High-temperature elasticity of iron-bearing olivines. *Journal of Geophysical Research*, *97*(B2), 1871–1885. https//doi.org/10.1029/91JB02675
Jackson, I., Faul, U. H., & Skelton, R. (2014). Elastically accommodated grain-boundary sliding: New insights from experiment and modeling. *Physics of the Earth and Planetary Interiors*, *228*, 203–210. https//doi.org/10.1016/j.pepi.2013.11.014
Jackson, I., Faul, U. H., Suetsugu, D., Bina, C., Inoue, T., & Jellinek, M. (2010). Grainsize-sensitive viscoelastic relaxation in olivine: Towards a robust laboratory-based model for seismological application. *Physics of the Earth and Planetary Interiors*, *183*(1-2), 151–163. https//doi.org/10.1016/j.pepi.2010.09.005
Jain, C., Korenaga, J., & Karato, S. (2018). On the grain size sensitivity of olivine rheology. *Journal of Geophysical Research: Solid Earth*, *123*, 674–688. https//doi.org/10.1002/2017JB014847
Jarvis, G., & Peltier, W. (1986). Lateral heterogeneity in the convecting mantle. *Journal of Geophysical Research*, *91*(B1), 435–451.
Jones, A. G., Afonso, J. C., & Fullea, J. (2017). Geochemical and geophysical constrains on the dynamic topography of the Southern African Plateau. *Geochemistry, Geophysics, Geosystems*, *18*, 3556–3575. https//doi.org/10.1002/2017GC006908
Jordan, T. H. (1975). The continental tectosphere. *Reviews of Geophysics*, *13*(3), 1–12.
Jordan, T. H. (1978). Composition and development of the continental tectosphere. *Nature*, *274*(5671), 544–548.
Karato, S. (1993). Importance of anelasticity in the interpretation of seismic tomography. *Geophysical Research Letters*, *20*(15), 1623–1626.
Karato, S. (2010). Rheology of the deep upper mantle and its implications for the preservation of the continental roots: A review. *Tectonophysics*, *481*(1), 82–98. https//doi.org/10.1016/j.tecto.2009.04.011
Karato, S., & Jung, H. (1998). Water, partial melting and the origin of the seismic low velocity and high attenuation zone in the upper mantle. *Earth and Planetary Science Letters*, *157*(3-4), 193–207. https//doi.org/10.1016/S0012-821X(98)00034-X
Karato, S., & Wu, P. (1993). Rheology of the upper mantle: A synthesis. *Science*, *260*(5109), 771–778.
Katz, R. F., Spiegelman, M., & Langmuir, C. H. (2003). A new parameterization of hydrous mantle melting. *Geochemistry, Geophysics, Geosystems*, *4*(9), 1073. https//doi.org/10.1029/2002GC000433
Klein, E. M., & Langmuir, C. H. (1987). Global correlations of ocean ridge basalt chemistry with axial depth and crustal thickness. *Journal of Geophysical Research*, *92*(B8), 8089–8115. https//doi.org/10.1029/95JB01460
Koelemeijer, P., Schuberth, B., Davies, D., Deuss, A., & Ritsema, J. (2018). Constraints on the presence of post-perovskite in Earth's lowermost mantle from tomographic-geodynamic model comparisons. *Earth and Planetary Science Letters*, *494*, 226–238. https//doi.org/10.1016/j.epsl.2018.04.056
Kohlstedt, D. L., Evans, B., & Mackwell, S. J. (1995). Strength of the lithosphere: Constraints imposed by laboratory experiments. *Journal of Geophysical Research*, *100*(B9), 17,587–17,602. https//doi.org/10.1029/95JB01460
Korenaga, T., & Korenaga, J. (2016). Evolution of young oceanic lithosphere and the meaning of seafloor subsidence rate. *Journal of Geophysical Research: Solid Earth*, *121*, 6315–6332. https//doi.org/10.1002/2016JB013395
Kumazawa, M., & Anderson, O. L. (1969). Elastic moduli, pressure derivatives, and temperature derivatives of single-crystal olivine and single-crystal forsterite. *Journal of Geophysical Research*, *74*(25), 5961–5972.
Kustowski, B., Ekström, G., & Dziewoński, A. M. (2008). Anisotropic shear-wave velocity structure of the Earth's mantle: A global model. *Journal of Geophysical Research*, *113*, B06306. https//doi.org/10.1029/2007JB005169
Lambeck, K., Smither, C., & Johnston, P. (1998). Sea-level change, glacial rebound and mantle viscosity for northern Europe. *Geophysical Journal International*, *134*(1), 102–144.
Lau, H. C., & Holtzman, B. K. (2019). "Measures of dissipation in viscoelastic media" extended: Toward continuous characterization across very broad geophysical time scales. *Geophysical Research Letters*, *46*, 9544–9553. https//doi.org/10.1029/2019GL083529
Lau, H. C. P., Mitrovica, J. X., Austermann, J., Crawford, O., Al-Attar, D., & Latychev, K. (2016). Inferences of mantle viscosity based on ice age data sets: Radial structure. *Journal of Geophysical Research: Solid Earth*, *121*, 6991–7012. https//doi.org/10.1002/2016JB013043
Lau, H. C., Mitrovica, J. X., Davis, J. L., Tromp, J., Yang, H. Y., & Al-Attar, D. (2017). Tidal tomography constrains Earth's deep-mantle buoyancy. *Nature*, *551*(7680), 321–326. https//doi.org/10.1038/nature24452
Lin, P.-Y. P., Gaherty, J. B., Jin, G., Collins, J. A., Lizarralde, D., Evans, R. L., & Hirth, G. (2016). High-resolution seismic constraints on flow dynamics in the oceanic asthenosphere. *Nature*, *535*(7613), 538. https//doi.org/10.1038/nature18012
Ma, Z., & Dalton, C. A. (2019). Evidence for dehydration-modulated small-scale convection in the oceanic upper mantle from seafloor bathymetry and Rayleigh wave phase velocity. *Earth and Planetary Science Letters*, *510*, 12–25.
Ma, Z., Dalton, C. A., Russell, J. B., Gaherty, J. B., Hirth, G., & Forsyth, D. W. (2020). Shear attenuation and anelastic mechanisms in the central Pacific upper mantle. *Earth and Planetary Science Letters*, *536*, 116,148.
Mao, Z., Fan, D., Lin, J.-F., Yang, J., Tkachev, S. N., Zhuravlev, K., & Prakapenka, V. B. (2015). Elasticity of single-crystal olivine at high pressures and temperatures. *Earth and Planetary Science Letters*, *426*, 204–215.
Mather, K. A., Pearson, D. G., McKenzie, D., Kjarsgaard, B. A., & Priestley, K. (2011). Constraints on the depth and thermal history of cratonic lithosphere from peridotite xenoliths, xenocrysts and seismology. *Lithos*, *125*(1-2), 729–742. https//doi.org/10.1016/j.lithos.2011.04.003
McCarthy, C., & Takei, Y. (2011). Anelasticity and viscosity of partially molten rock analogue: Toward seismic detection of small quantities of melt. *Geophysical Research Letters*, *38*, L18306. https//doi.org/10.1029/2011GL048776
McCarthy, C., Takei, Y., & Hiraga, T. (2011). Experimental study of attenuation and dispersion over a broad frequency range: 2. The universal scaling of polycrystalline materials. *Journal of Geophysical Research*, *116*, B09207. https//doi.org/10.1029/2011JB008384
McKenzie, D. (2000). Constraints on melt generation and transport from U-series activity ratios. *Chemical Geology*, *162*(2), 81–94.
Menard, H. W. (1973). Depth anomalies and the bobbing motion of drifting islands. *Journal of Geophysical Research*, *78*(23), 5128–5137. https//doi.org/10.1029/JB078i023p05128
Mitrovica, J. X., & Forte, A. M. (2004). A new inference of mantle viscosity based upon joint inversion of convection and glacial isostatic adjustment data. *Earth and Planetary Science Letters*, *225*(1-2), 177–189. https//doi.org/10.1016/j.epsl.2004.06.005
Molnar, P., England, P. C., & Jones, C. H. (2015). Mantle dynamics, isostasy, and the support of high terrain. *Journal of Geophysical Research: Solid Earth*, *120*, 1932–1957. https//doi.org/10.1002/2014JB011724
Morgan, J. P., & Smith, W. H. (1992). Flattening of the sea-floor depth-age curve as a response to asthenospheric flow. *Nature*, *359*(6395), 524.

Natarov, S. I., & Conrad, C. P. (2012). The role of Poiseuille flow in creating depth-variation of asthenospheric shear. *Geophysical Journal International*, *190*(3), 1297–1310. https//doi.org/10.1111/j.1365-246X.2012.05562.x
Osei Tutu, A., Sobolev, S. V., Steinberger, B., Popov, A. A., & Rogozhina, I. (2018). Evaluating the influence of plate boundary friction and mantle viscosity on plate velocities. *Geochemistry, Geophysics, Geosystems*, *19*, 642–666. https//doi.org/10.1002/2017GC007112
Panasyuk, S. V., & Hager, B. H. (2000). Models of isostatic and dynamic topography, geoid anomalies, and their uncertainties. *Journal of Geophysical Research*, *105*(B12), 28,199–28,209. https//doi.org/10.1029/2000JB900249
Parsons, B., & Sclater, J. G. (1977). An analysis of the variation of ocean floor bathymetry and heat flow with age. *Journal of Geophysical Research*, *82*(5), 803–827. https//doi.org/10.1029/JB082i005p00803
Phipps Morgan, J., Morgan, W. J., Zhang, Y.-S., & Smith, W. H. F. (1995). Observational hints for a plume-fed, suboceanic asthenosphere and its role in mantle convection. *Journal of Geophysical Research*, *100*(B7), 12,753–12,767. https//doi.org/10.1029/95JB00041
Press, W. H., Teukolsky, S. A., Vetterling, W. T., Flannery, B. P., & (1992). *Numerical recipes in C: The art of scientific computing* (2nd). New York, NY, USA: Cambridge University Press.
Priestley, K., & McKenzie, D. (2006). The thermal structure of the lithosphere from shear wave velocities. *Earth and Planetary Science Letters*, *244*(1-2), 285–301. https//doi.org/10.1016/j.epsl.2006.01.008
Priestley, K., & McKenzie, D. (2013). The relationship between shear wave velocity, temperature, attenuation and viscosity in the shallow part of the mantle. *Earth and Planetary Science Letters*, *381*, 78–91. https//doi.org/10.1016/j.epsl.2013.08.022
Priestley, K., McKenzie, D., Barron, J., Tatar, M., & Debayle, E. (2012). The Zagros core: Deformation of the continental lithospheric mantle. *Geochemistry, Geophysics, Geosystems*, *13*, Q11014. https//doi.org/10.1029/2012GC004435
Rawlinson, N., Fichtner, A., Sambridge, M., & Young, M. K. (2014). Seismic tomography and the assessment of uncertainty. *Advances in Geophysics*, *55*, 1–76.
Ricard, Y., Richards, M., Lithgow-Bertelloni, C., & Le Stunff, Y. (1993). A geodynamic model of mantle density heterogeneity. *Journal of Geophysical Research*, *98*(B12), 21,895–21,909. https//doi.org/10.1029/93JB02216
Richards, M. A., & Hager, B. H. (1984). Geoid anomalies in a dynamic Earth. *Journal of Geophysical Research*, *89*(B7), 5987–6002. https//doi.org/10.1029/JB089iB07p05987
Richards, F. D., Hoggard, M. J., Cowton, L. R., & White, N. J. (2018). Reassessing the thermal structure of oceanic lithosphere with revised global inventories of basement depths and heat flow measurements. *Journal of Geophysical Research: Solid Earth*, *123*, 9136–9161. https//doi.org/10.1029/2018JB015998
Rickers, F., Fichtner, A., & Trampert, J. (2013). The Iceland-Jan Mayen plume system and its impact on mantle dynamics in the North Atlantic region: Evidence from full-waveform inversion. *Earth and Planetary Science Letters*, *367*, 39–51. https//doi.org/10.1016/j.epsl.2013.02.022
Ridout, M. S. (2009). Statistical applications of the complex-step method of numerical differentiation. *The American Statistician*, *63*(1), 66–74.
Ritsema, J., Deuss, A., Van Heijst, H. J., & Woodhouse, J. H. (2011). S40RTS: A degree-40 shear-velocity model for the mantle from new Rayleigh wave dispersion, teleseismic traveltime and normal-mode splitting function measurements. *Geophysical Journal International*, *184*, 1223–1236. https//doi.org/10.1111/j.1365-246X.2010.04884.x
Ritsema, J., van Heijst, H. J., & Woodhouse, J. H. (1999). Complex shear wave velocity structure imaged beneath Africa and Iceland. *Science*, *286*(5446), 1925–1928. https//doi.org/10.1126/science.286.5446.1925
Ritzwoller, M. H., Shapiro, N. M., & Zhong, S.-J. (2004). Cooling history of the Pacific lithosphere. *Earth and Planetary Science Letters*, *226*(1-2), 69–84.
Robinson, E. M., Parsons, B., & Daly, S. F. (1987). The effect of a shallow low viscosity zone on the apparent compensation of mid-plate swells. *Earth and Planetary Science Letters*, *82*(3), 335–348. https//doi.org/10.1016/0012-821X(87)90207-X
Schaeffer, A. J., & Lebedev, S. (2013). Global shear speed structure of the upper mantle and transition zone. *Geophysical Journal International*, *194*(1), 417–449. https//doi.org/10.1093/gji/ggt095
Schuberth, B. S. A., & Bunge, H. P. (2009). Tomographic filtering of high-resolution mantle circulation models: Can seismic heterogeneity be explained by temperature alone? *Geochemistry, Geophysics, Geosystems*, *10*, Q05W03. https//doi.org/10.1029/2009GC002401
Schutt, D. L., & Lesher, C. E. (2006). Effects of melt depletion on the density and seismic velocity of garnet and spinel lherzolite. *Journal of Geophysical Research*, *111*, B05401. https//doi.org/10.1029/2003JB002950
Semple, A. G., & Lenardic, A. (2018). Plug flow in the Earth's asthenosphere. *Earth and Planetary Science Letters*, *496*, 29–36.
Shapiro, S. S., Hager, B. H., & Jordan, T. H. (1999). The continental tectosphere and Earth's long-wavelength gravity field. *Lithos*, *48*(1-4), 135–152.
Shorttle, O., Maclennan, J., & Lambart, S. (2014). Quantifying lithological variability in the mantle. *Earth and Planetary Science Letters*, *395*, 24–40. https//doi.org/10.1016/j.epsl.2014.03.040
Simmons, N. A., Forte, A. M., & Grand, S. P. (2009). Joint seismic, geodynamic and mineral physical constraints on three-dimensional mantle heterogeneity: Implications for the relative importance of thermal versus compositional heterogeneity. *Geophysical Journal International*, *177*(3), 1284–1304.
Spasojevic, S., & Gurnis, M. (2012). Sea level and vertical motion of continents from dynamic Earth models since the Late Cretaceous. *AAPG Bulletin*, *96*(11), 2037–2064. https//doi.org/10.1306/03261211121
Steinberger, B. (2007). Effects of latent heat release at phase boundaries on flow in the Earth's mantle, phase boundary topography and dynamic topography at the Earth's surface. *Physics of the Earth and Planetary Interiors*, *164*(1-2), 2–20. https//doi.org/10.1016/j.pepi.2007.04.021
Steinberger, B. (2016). Topography caused by mantle density variations: Observation-based estimates and models derived from tomography and lithosphere thickness. *Geophysical Journal International*, *205*(1), 604–621. https//doi.org/10.1093/gji/ggw040
Steinberger, B., & Calderwood, A. R. (2006). Models of large-scale viscous flow in the Earth's mantle with constraints from mineral physics and surface observations. *Geophysical Journal International*, *167*(3), 1461–1481. https//doi.org/10.1111/j.1365-246X.2006.03131.x
Steinberger, B., Conrad, C. P., Tutu, A. O., & Hoggard, M. J. (2017). On the amplitude of dynamic topography at spherical harmonic degree two. *Tectonophysics*, *760*, 221–228. https//doi.org/10.1016/j.tecto.2017.11.032
Steinberger, B., Werner, S. C., & Torsvik, T. H. (2010). Deep versus shallow origin of gravity anomalies, topography and volcanism on Earth, Venus and Mars. *Icarus*, *207*(2), 564–577. https//doi.org/10.1016/j.icarus.2009.12.025
Stixrude, L., & Lithgow-Bertelloni, C. (2005). Mineralogy and elasticity of the oceanic upper mantle: Origin of the low-velocity zone. *Journal of Geophysical Research*, *110*, B03204. https//doi.org/10.1029/2004JB002965
Stixrude, L., & Lithgow-Bertelloni, C. (2011). Thermodynamics of mantle minerals—II. Phase equilibria. *Geophysical Journal International*, *184*(3), 1180–1213. https//doi.org/10.1111/j.1365-246X.2010.04890.x

Stixrude, L., & Lithgow-Bertelloni, C. (2012). Geophysics of chemical heterogeneity in the mantle. *Annual Review of Earth and Planetary Sciences*, *40*(1), 569–595. https//doi.org/10.1146/annurev.earth.36.031207.124244

Stotz, I. L., Iaffaldano, G., & Davies, D. R. (2018). Pressure-driven Poiseuille flow: A major component of the torque-balance governing Pacific plate motion. *Geophysical Research Letters*, *45*, 117–125. https//doi.org/10.1002/2017GL075697

Takei, Y. (2017). Effects of partial melting on seismic velocity and attenuation: A new insight from experiments. *Annual Review of Earth and Planetary Sciences*, *45*, 1–25. https//doi.org/10.1146/annurev-earth-063016-015820

Takei, Y., Karasawa, F., & Yamauchi, H. (2014). Temperature, grain size, and chemical controls on polycrystal anelasticity over a broad frequency range extending into the seismic range. *Journal of Geophysical Research: Solid Earth*, *119*, 5414–5443. https//doi.org/10.1002/2014JB011146

Thomson, A. R., Walter, M. J., Kohn, S. C., & Brooker, R. A. (2016). Slab melting as a barrier to deep carbon subduction. *Nature*, *529*(7584), 76–79. https//doi.org/10.1017/CBO9781107415324.004

van der Wal, W., Whitehouse, P. L., & Schrama, E. J. O. (2015). Effect of GIA models with 3D composite mantle viscosity on GRACE mass balance estimates for antarctica. *Earth and Planetary Science Letters*, *414*, 134–143. https//doi.org/10.1016/j.epsl.2015.01.001

Wen, L., & Anderson, D. L. (1997). Slabs, hotspots, cratons and mantle convection revealed from residual seismic tomography in the upper mantle. *Physics of the Earth and Planetary Interiors*, *99*(96), 131–143. https//doi.org/10.1016/S0031-9201(96)03162-7

White, R. S., McKenzie, D., & O'Nions, R. K. (1992). Oceanic crustal thickness from seismic measurements and rare earth element inversions. *Journal of Geophysical Research*, *97*(B13), 19,683–19,715. https//doi.org/10.1029/92JB01749

Winterbourne, J. R., Crosby, A. G., & White, N. J. (2009). Depth, age and dynamic topography of oceanic lithosphere beneath heavily sedimented Atlantic margins. *Earth and Planetary Science Letters*, *287*, 137–151. https//doi.org/10.1016/j.epsl.2009.08.019

Winterbourne, J., White, N., & Crosby, A. (2014). Accurate measurements of residual topography from the oceanic realm. *Tectonics*, *33*(6), 982–1015. https//doi.org/10.1002/2013TC003372

Yamauchi, H., & Takei, Y. (2016). Polycrystal anelasticity at near-solidus temperatures. *Journal of Geophysical Research: Solid Earth*, *121*, 7790–7820. https//doi.org/10.1002/2016JB013316

Yang, T., & Gurnis, M. (2016). Dynamic topography, gravity and the role of lateral viscosity variations from inversion of global mantle flow. *Geophysical Journal International*, *207*(2), 1186–1202. https//doi.org/10.1093/gji/ggw335

Zhang, S., & Karato, S. (1995). Lattice preferred orientation of olivine aggregates deformed in simple shear. *Nature*, *375*(6534), 774–777.

Zhong, S., & Davies, G. F. (1999). Effects of plate and slab viscosities on the geoid. *Earth and Planetary Science Letters*, *170*(4), 487–496.